RSC Advances

PAPER

View Article Online
View Journal | View Issue

Cite this: *RSC Adv.*, 2023, **13**, 13624

Modeling of magnesium-decorated graphene quantum dot nanostructure for trapping AsH_3, PH_3 and NH_3 gases†

Ernest C. Agwamba, *[acd] Hitler Louis, *[ab] Praise O. Olagoke,[a] Terkumbur E. Gber, [ab] Gideon A. Okon,[a] Chidera F. Fidelis[ab] and Adedapo S. Adeyinka[d]

A magnesium-decorated graphene quantum dot ($C_{24}H_{12}$-Mg) surface has been examined theoretically using density functional theory (DFT) computations at the ωB97XD/6-311++G(2p,2d) level of theory to determine its sensing capability toward XH_3 gases, where X = As, N and P, in four different phases: gas, benzene solvent, ethanol solvent and water. This research was carried out in different phases in order to predict the best possible phase for the adsorption of the toxic gases. Analysis of the electronic properties shows that in the different phases the energy gap follows the order NH_3@$C_{24}H_{12}$-Mg < PH_3@$C_{24}H_{12}$-Mg < AsH_3@$C_{24}H_{12}$-Mg. The results obtained from the adsorption studies show that all the calculated adsorption energies are negative, indicating that the nature of the adsorption is chemisorption. The adsorption energies can be arranged in an increasing trend of NH_3@$C_{24}H_{12}$-Mg < PH_3@$C_{24}H_{12}$-Mg < AsH_3@$C_{24}H_{12}$-Mg. The best adsorption performance was noted in the gas phase compared to the other studied counterparts. The interaction between the adsorbed gases and the surfaces shows a non-covalent interaction nature, as confirmed by the quantum theory of atoms-in-molecules (QTAIM) and non-covalent interactions (NCI) analysis. The overall results suggest that we can infer that the surface of the magnesium-decorated graphene quantum dot $C_{24}H_{12}$-Mg is more efficient for sensing the gas AsH_3 than PH_3 and NH_3.

Received 24th February 2023
Accepted 18th April 2023

DOI: 10.1039/d3ra01279d

rsc.li/rsc-advances

1 Introduction

Recent advances in nanomaterial science have improved the concept of gas sensors[1] and furthermore created an increase in the potential for designing efficient, effective and selective gas sensors for identifying and sensing volatile and hazardous gases.[2–4] Several nanostructured materials have been considered by researchers due to their outstanding features, such as high selectivity, good stability, low toxicity, high surface activity, quick recovery, high sensitivity, fast response, low operating temperature, and pronounced quantum confinement.[5–7] Graphene quantum dots, which are graphene nanoparticle materials having a size of less than 100 nm, have drawn the attention of researchers owing to their excellent sensing properties.[8,9] Graphene quantum dots possesses good structural, electronic, spin optical and photoelectric features.[10] In addition to their uses in sensors, they are also applicable in solar cells, photodetectors, drug delivery, bioimaging and photoluminescent materials.[11–13] The promising properties of graphene quantum dots in sensing have been reviewed and reported. As reported by Meixiu Li *et al.*,[14] graphene quantum dots exhibit high photostability against blinking and photo-leaching, as well as low toxicity, and thus have greater biocompatibility. Graphene quantum dot materials for sensing, bioimaging and energy storage applications have been reviewed by Kumar *et al.*[15]

Recently, the density functional theory (DFT) method has been invoked for theoretical calculations to examine and predict the properties of materials under investigation.[16,17] This method is an important method in the scientific community today, and it can help to determine whether a nanomaterial could be considered for sensing applications.[18] DFT methodology can be also employed to gain insight into a gas sensor material to understand the molecular electronic and structural properties, mechanistic behavior, conductivity, and sensitivity of the material to detect and identify hazardous gases such as AsH_3, NH_3, PH_3.[19–21] Arsine (AsH_3), ammonia (NH_3) and phosphine (PH_3) are toxic colorless hydride gases with a pungent smell.[22,23] They are highly irritating gases that are also

[a]*Computational and Bio-Simulation Research Group, University of Calabar, Calabar, Nigeria. E-mail: Agwamba.Ernest@gmail.com; gberterkumburemmanuel@gmail.com*
[b]*Department of Pure and Applied Chemistry, Faculty of Physical Sciences, University of Calabar, Calabar, Nigeria*
[c]*Department of Chemistry, Covenant University, Otta, Nigeria*
[d]*Department of Chemical Sciences, University of Johannesburg, Johannesburg, South Africa*

† Electronic supplementary information (ESI) available. See DOI: https://doi.org/10.1039/d3ra01279d

flammable.[23] Exposure to these gases can cause skin irritation, headache, vomiting, nausea, and pains.[24–26] Inhalation of large concentrations of these gases can cause liver, kidney or nerve damage and can lead to death.[27–29] Hence, it is of utmost importance that these gases should be sensed or detected.[30] Numerous efforts have been made through the density functional theory (DFT) method towards the sensing and adsorption of XH_3 (X = As, N, P) gases using a graphene or graphene-like structure. NH_3, PH_3, and AsH_3 adsorption and sensing on alkaline earth metal (AEM = Be, Mg, Ca and Sr)-doped graphene was conducted by Singsen *et al.*[31] Their results revealed that the gases were weakly absorbed on intrinsic graphene. On the doped structures, significant increases in the charge transfer, adsorption energies and orbital hybridization of the systems were observed. The Mg-doped graphene showed sensitivity towards PH_3 and AsH_3 in the sensitivity response and recovery time analysis, while the Sr-doped graphene revealed sensitivity towards NH_3. Luo *et al.*[32] also studied the sensing and adsorption of AsH_3, NH_3, and PH_3 on rare-earth-metal-doped graphene through the DFT method. Their study showed that the graphene exhibited physisorption towards the gases. No significant changes were observed in the geometry, density of states or charge population of the structure. However, upon modification by a rare-earth metal, enhanced chemisorption of the gases was observed Luo *et al.*[33] conducted a DFT investigation of NH_3, PH_3 and AsH_3 adsorption on Sc-, Tl-, V-, and Cr-doped single-wall carbon nanotubes (SWCNT). Their adsorption ability followed the order NH_3 > PH_3 > AsH_3. Their study showed that the transition metal (TM)-doped SWCNTs were more favorable for gas sensing and adsorption than the pristine SWCNTs. Based on various studies, it can be deduced that structural modification such as doping, encapsulation or decoration of a material can enhance its properties to make it a better gas sensing material.

However, to the best of our knowledge there have been no studies involving the theoretical investigation of the sensing of hydride gases using graphene quantum dots in different phases and solvation states. Additionally, the detection and removal of toxic gases such as AsH_3, PH_3, and NH_3 is of critical importance due to their harmful effects on the environment and human health. Magnesium-decorated graphene quantum dot nanostructures have shown promising potential for trapping these gases, but a comprehensive understanding of their behavior and efficacy is lacking. Therefore, the research problem is to model the interaction of AsH_3, PH_3, and NH_3 with magnesium-decorated graphene quantum dot nanostructures and investigate the factors influencing their gas sensing performance. In this paper, the density functional theory (DFT) method with the WB97XD functional and 6-311++G(2p,2d) basis set has been employed to study and analyze the selectivity, sensitivity, conductivity and efficacy of a graphene quantum dot and its decorated magnesium atom in sensing the toxic hydride gases XH_3, where X = As, N and P. This study was carried out in four different phases, namely, gas, benzene, ethanol and water, to provide insights into the effect of solvation and to determine the best possible phase for the adsorption of the gases. The following analyses were carried out in this study: structural properties, frontier molecular orbital (FMO), density of states (DOS), natural bond orbital (NBO), quantum theory of atoms-in-molecules (QTAIM), non-covalent interactions (NCI), adsorption study, sensor mechanics, electrical conductivity, recovery time and work function, dipole moment and charge transfer, nonlinear optics (NLO) analysis and thermodynamics properties. The FMO parameters and the DOS were invoked to study the molecular electronic properties of the magnesium-decorated graphene quantum dots. QTAIM and NCI were utilized to verify the non-covalent interactions existing within the adsorbate and adsorbent. Comparative adsorption energy and sensor mechanisms were employed in this study to determine the sensing ability of the studied surfaces and the adsorbate.

2 Computational details

The density functional theory (DFT) method was employed to handle all theoretical calculations performed on the studied surface of the graphene quantum dot with its decorated magnesium atom. The calculations were achieved with the Gaussview 6.0.16 (ref. 34) and Gaussian 16 suite of programs[35] using the hybrid long-range separated empirical-correlated dispersion ωB97XD functional and the 6-311++G(2p,2d) basis set. The calculations were first carried out in vacuum, which is the gas phase, before further calculations were made for solvation with benzene, ethanol and water. Local minima on the potential energy surface were achieved by considering the frequency calculation at the same level of theory. Thus, the absence of imaginary frequencies confirmed the absolute correspondence of the optimized geometry to a local minimum on the potential energy surface.[36,37] The structural properties were achieved *via* the software Chemcraft 16.[38] The frontier molecular orbital (FMO), which analyses the conductivity and stability of the magnesium-decorated graphene quantum dots, was carried out. The highest occupied molecular orbital (HOMO) and lowest unoccupied molecular orbital (LUMO) energy values were obtained through Gaussian 16 and further calculations of the quantum descriptors were calculated with the aid of Koopmans' approximation.[39] The pictorial representations of the HOMO and LUMO iso-surfaces were obtained *via* Chemcraft. The software Origin[40] was used to plot the graphical representation of the density of states (DOS). Using the same functional and basis set, the natural bond orbital (NBO) calculations were carried out using the NBO 3.0 (ref. 41) embedded in the Gaussian 16 software. The quantum theory of atoms in molecules and non-covalent interaction analysis was achieved *via* the multifunctional wave function analyzer program multiwfn 3.0.[42] Pictorial representations of the QTAIM and NCI were obtained using Visual Molecular Dynamics (VMD).[43] The absorption energies of the gases adsorbed on the $C_{24}H_{12}$-Mg quantum dot surface were calculated using eqn (1):

$$E_{ads} = E_{C_{24}H_{12}\text{-Mg/gas}} - (E_{gas} + E_{C_{24}H_{12}\text{-Mg}}) \quad (1)$$

where E_{ads} = absorption energy of the gases on the magnesium-decorated graphene quantum dot surface. $E_{C_{24}H_{12}\text{-Mg/gas}}$ = Total

energy of the structure after absorption of the XH_3 (X = As, N, P) on the magnesium-decorated graphene quantum dots surface. E_{gas} = energy of each of the isolated gases. $E_{C_{24}H_{12}\text{-}Mg}$ = energy of the magnesium-decorated graphene quantum dots surface.

3 Results and discussions

3.1 Structural properties

Insight into the structural configuration of studied structures can be obtained by proper structural and geometrical optimization.[44] In this work, all the structures of the adsorbed gases on the magnesium-decorated graphene quantum dot in the four different phases (gas, benzene, ethanol and water) were optimized using the DFT/ωB97XD/6-311++G(2p,2d) method. The optimized structures of magnesium-decorated graphene quantum dot as absorbent and the studied gases AsH_3, NH_3, and PH_3 are presented in Fig. 1. The graphene quantum dot comprises seven hexagons, which makes it a hexagonal structure.[45] AsH_3, NH_3 and PH_3 have a tetrahedral geometry and trigonal pyramidal shapes.[46] The bond distance between the gases and the quantum dot is an important parameter that reveals details about the strength of the material and can also determine the kind of bond formation.[47] The bond lengths of the quantum dot before and after the adsorption of the gases have been evaluated and computed in Table 1. Before adsorption of the gases on the adsorbent, it is observed that the bond length of magnesium to carbon (Mg–C) is in the range of 3.7–6.1 Å. For the gas phase, the shortest bond length between the magnesium atom and carbon atom is 3.745 Å, occurring for Mg_{37}–C_{18}. For the benzene phase, the bond length between the quantum dot and the magnesium atom is observed to be 3.963 Å for Mg_{37}–C_{22}, while it is found to be 3.981 Å and 3.986 Å for the ethanol and water phases, respectively, for Mg_{37}–C_{18}. After the interaction of the bare surface of the quantum dot and the investigated gas, it is noted that there is an effect on the geometrical bond length of the surface, especially between the magnesium and carbon atom. It is observed that there is a slight difference in the magnesium–carbon bond length in all phases. Upon the adsorption of AsH_3 on the surface, the bond length of magnesium to carbon 18, Mg_{37}–C_{18}, exhibited a shift in value from 3.745 Å to 3.757 Å, 3.963 Å to 3.954 Å, 3.981 Å to 3.977 Å, and from 3.986 Å to 3.977 Å in the gas, benzene, ethanol and water phase, respectively. For NH_3, it is observed that the shortest bond length of magnesium to carbon atom was recorded to be 3.825 Å, 3.966 Å, 3.972 Å, 4.016 Å corresponding to gas, benzene, ethanol, and water phase, respectively. Similarly, for PH_3, there is also a change in the values of the length of the bond existing between the magnesium and carbon atom, which is found to be 3.789 Å for the gas phase, 3.963 Å for benzene, 4.000 Å for ethanol and 3.999 Å for water. The differences occurring upon adsorption of the investigated gases on the surface of the magnesium-decorated graphene quantum dot are the result of charge transfer occurring between the adsorbate (investigated gases) and the adsorbent (the quantum dot). There is the formation of a bond in the structure between the gases and the surface after the adsorption process. In the gas phase, $AsH_3@C_{24}H_{12}$-Mg is noted to have a bond length of 3.734 Å for As_{37}–C_{19}. The shortest bond length formed between the nitrogen and carbon atom in the case of $NH_3@C_{24}H_{12}$-Mg for the gas phase is recorded to be 3.565 Å. For $PH_3@C_{24}H_{12}$-Mg in the gas phase, the bond label of P_{41}–C_{13} corresponds to a bond length of 3.470 Å. Examining the bond length between the different gases and the surface in the gas phase, it can be deduced that $PH_3@C_{24}H_{12}$-Mg has the shortest bond length. Observations from the benzene, ethanol and water phases show $AsH_3@C_{24}H_{12}$-Mg to have the longest bond length and

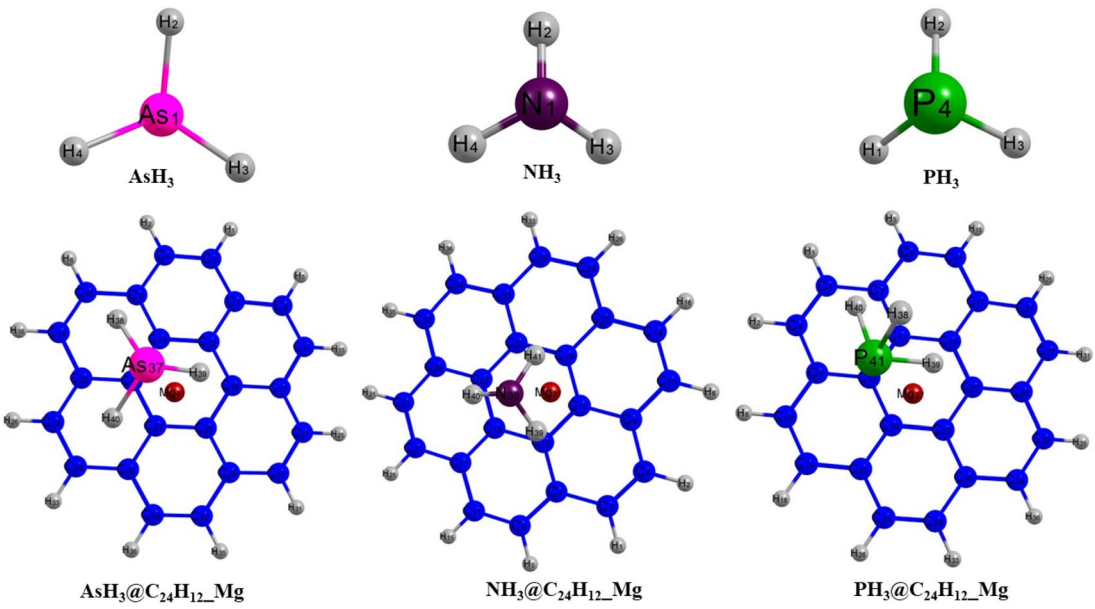

Fig. 1 Pictorial representation of AsH_3, NH_3 and PH_3, and the gas-adsorbed surfaces of $AsH_3@C_{24}H_{12}$-Mg, $NH_3@C_{24}H_{12}$-Mg and $PH_3@C_{24}H_{12}$-Mg.

Table 1 Selected bond lengths of the investigated system with DFT/ωB97XD/6-311++G(2p,2d) method

	System							
	$C_{24}H_{12}$-Mg		$AsH_3@C_{24}H_{12}$-Mg		$NH_3@C_{24}H_{12}$-Mg		$PH_3@C_{24}H_{12}$-Mg	
Phases	Bond label	Bond length (Å)	Bond label	Bond length (Å)	Bond label	Bond length (Å)	Bond label	Bond length (Å)
Gas	Mg_{37}–C_{18}	3.745	As_{37}–H_{39}	1.517	N_{38}–H_{39}	1.012	P_{41}–H_{39}	1.414
	C_{18}–C_{17}	1.406	As_{37}–C_{19}	3.734	N_{38}–C_{13}	3.565	P_{41}–C_{13}	3.470
	C_{18}–C_{12}	1.423	C_{19}–C_{20}	1.405	C_{13}–C_9	1.405	C_{13}–C_9	1.405
	C_{18}–C_{22}	1.423	Mg_{41}–C_{18}	3.757	Mg_{37}–C_{18}	3.825	Mg_{37}–C_{22}	3.789
Benzene	Mg_{37}–C_{22}	3.963	As_{37}–H_{39}	1.516	N_{38}–H_{39}	1.013	P_{41}–H_{39}	1.415
	C_{22}–C_{28}	1.406	As_{37}–C_{20}	4.066	N_{38}–C_{13}	3.594	P_{41}–C_{13}	3.471
	C_{22}–C_{18}	1.422	C_{20}–C_{24}	1.420	C_{13}–C_9	1.406	C_{13}–C_9	1.406
	C_{22}–C_{28}	1.422	Mg_{41}–C_{18}	3.954	Mg_{37}–C_{19}	3.966	Mg_{37}–C_{23}	3.963
Ethanol	Mg_{37}–C_{18}	3.981	As_{37}–H_{39}	1.516	N_{38}–H_{39}	1.014	P_{41}–H_{39}	1.413
	C_{18}–C_{17}	1.406	As_{37}–C_{19}	3.737	N_{38}–C_{18}	3.651	P_{41}–C_{13}	3.460
	C_{18}–C_{12}	1.422	C_{19}–C_{20}	1.405	C_{18}–C_{17}	1.406	C_{13}–C_9	1.406
	C_{18}–C_{22}	1.422	Mg_{41}–C_{18}	3.977	Mg_{37}–C_{13}	3.972	Mg_{37}–C_{23}	4.000
Water	Mg_{37}–C_{18}	3.986	As_{37}–H_{39}	1.516	N_{38}–H_{40}	1.014	P_{41}–H_{39}	1.413
	C_{18}–C_{17}	1.406	As_{37}–C_{23}	3.945	N_{38}–C_{13}	3.593	P_{41}–C_{13}	3.460
	C_{18}–C_{12}	1.423	C_{23}–C_{30}	1.406	C_{13}–C_9	1.406	C_{13}–C_9	1.406
	C_{18}–C_{22}	1.423	Mg_{41}–C_{18}	3.977	Mg_{37}–C_{22}	4.016	Mg_{37}–C_{23}	3.999

$PH_3@C_{24}H_{12}$-Mg to have the shortest bond length. Therefore, for all the phases, it can be said that the structure in terms of bond length follows an increasing trend of $PH_3@C_{24}H_{12}$-Mg < $NH_3@C_{24}H_{12}$-Mg < $AsH_3@C_{24}H_{12}$-Mg. The bond lengths between As, N and P and their hydrogen atoms, as well as the shortest carbon-to-carbon bonds, are also recorded in Table 1.

3.2 Frontier molecular orbital (FMO)

For the purpose of analyzing the electron transfer, kinetic stability, conductivity and sensing ability of the magnesium-decorated graphene quantum dot, the frontier molecular orbital (FMO) has been computed.[48,49] The FMO serves as an approach for illustrating and understanding the electronic properties of a system.[50] The FMO is constituted by two important orbitals: the highest occupied molecular orbital (HOMO) and the lowest unoccupied molecular orbital (LUMO).[51,52] The highest occupied molecular (HOMO) and lowest unoccupied molecular orbital (LUMO) help to depict the chemical activity of molecules and are also closely related to the donation and acceptance of an electron within a molecule.[53,54] By default, the HOMO has higher tendency to donate an electron, while the LUMO has a higher tendency to accept an electron.[55] The HOMO and LUMO give rise to a very important parameter, which is called the energy gap.[56] The energy gap reveals details regarding the electron transfer, stability and electrical conductivity displayed by a structure.[57] The energy gap is obtained by calculating the difference between the HOMO and the LUMO, and can be expressed mathematically as eqn (2):

$$E_g = E_{LUMO} - E_{HOMO} \quad (2)$$

where E_g = energy gap, E_{LUMO} = energy of the LUMO and E_{HOMO} = energy of the HOMO.

In this study, the energies of the HOMO and LUMO were established using the DFT functional WB97XD with the 6-311++G (2d,2p) basis set, and their values are reported in Table 2. Here, the FMO analysis was computed on the bare surface of the magnesium-decorated graphene quantum dot and also on the gas-adsorbed magnesium-decorated graphene quantum dot for the four different phases, which are gas, benzene, ethanol and water. Before the adsorption of the studied gases on the surface, the bare surface of the magnesium-decorated graphene quantum dot was observed to have an energy gap of 6.340 eV with a HOMO value of −6.531 eV and LUMO of −0.190 eV for the gas phase. The energy gap for the benzene phase is 5.850 eV, and similarly, for the ethanol and the water phase, the energy gap of the bare surface of the quantum dot is 5.292 eV and 5.297 eV, respectively. Looking closely at Table 2, it can be observed that the surface of the magnesium-decorated graphene quantum dot has high energy gap values, indicating better stability of the surface. As presented in Table 2, it is observed that upon adsorption of the three gases in the different phases, there is a slight decrement in the values of the energy gap, except in the ethanol phase. According to some literature review, a decrease in energy gap indicates a good effect in conductivity of the surface, which is essential for the selective and effective sensing of the studied gases.[58] In the gas phase, it is noted that the highest energy gap value was obtained upon adsorption of phosphorus hydride (PH_3) on the magnesium-decorated graphene quantum dot, while the lowest energy gap was obtained for ammonia (NH_3). In the gas phase, the HOMO–LUMO gap (energy gap) increases in the order 6.302 eV < 6.313 eV < 6.317 eV for $NH_3@C_{24}H_{12}$-Mg < $AsH_3@C_{24}H_{12}$-Mg < $PH_3@C_{24}H_{12}$-Mg, respectively. For the benzene phase, upon adsorption of the studied gases, the lowest energy gap was found for $NH_3@C_{24}H_{12}$-Mg with a value of 5.818 eV. In the benzene phase, both $AsH_3@C_{24}H_{12}$-Mg and

Table 2 Quantum chemical parameters for the studied gases adsorbed on the $C_{24}H_{12}$-Mg quantum dot calculated using the DFT/ωB97XD/6-311++G(2p,2d) method

Phase	System	HOMO (eV)	LUMO (eV)	Energy gap	IP	EA	χ	μ	η	σ	ω
Gas	$C_{24}H_{12}$-Mg	−6.531	−0.190	6.340	6.531	0.190	3.361	−3.361	3.170	0.158	1.781
	AsH_3@$C_{24}H_{12}$-Mg	−6.553	−0.240	6.313	6.553	0.240	3.397	−3.397	3.157	0.158	1.827
	NH_3@$C_{24}H_{12}$-Mg	−6.617	−0.315	6.302	6.617	0.315	3.466	−3.466	3.151	0.159	1.906
	PH_3@$C_{24}H_{12}$-Mg	−6.551	−0.235	6.317	6.551	0.235	3.393	−3.393	3.158	0.158	1.822
Benzene	$C_{24}H_{12}$-Mg	−6.025	−0.174	5.850	6.025	0.174	3.099	−3.099	2.925	0.171	1.642
	AsH_3@$C_{24}H_{12}$-Mg	−6.033	−0.198	5.834	6.033	0.198	3.116	−3.116	2.917	0.171	1.664
	NH_3@$C_{24}H_{12}$-Mg	−6.064	−0.247	5.818	6.064	0.247	3.155	−3.155	2.909	0.172	1.711
	PH_3@$C_{24}H_{12}$-Mg	−6.034	−0.200	5.834	6.034	0.200	3.117	−3.117	2.917	0.171	1.666
Ethanol	$C_{24}H_{12}$-Mg	−5.524	−0.232	5.292	5.524	0.232	2.878	−2.878	2.646	0.189	1.565
	AsH_3@$C_{24}H_{12}$-Mg	−5.544	−0.230	5.314	5.544	0.230	2.887	−2.887	2.657	0.188	1.568
	NH_3@$C_{24}H_{12}$-Mg	−5.546	−0.250	5.297	5.546	0.250	2.898	−2.898	2.648	0.189	1.586
	PH_3@$C_{24}H_{12}$-Mg	−5.546	−0.250	5.297	5.546	0.250	2.898	−2.898	2.648	0.189	1.586
Water	$C_{24}H_{12}$-Mg	−5.546	−0.250	5.297	5.546	0.250	2.898	−2.898	2.648	0.189	1.586
	AsH_3@$C_{24}H_{12}$-Mg	−5.510	−0.237	5.273	5.510	0.237	2.873	−2.873	2.637	0.190	1.566
	NH_3@$C_{24}H_{12}$-Mg	−5.513	−0.252	5.262	5.513	0.252	2.883	−2.883	2.631	0.190	1.579
	PH_3@$C_{24}H_{12}$-Mg	−5.512	−0.259	5.254	5.512	0.259	2.885	−2.885	2.627	0.190	1.585

PH_3@$C_{24}H_{12}$-Mg have the same energy gap of 5.834 eV. In the ethanol phase, the highest energy gap was observed in AsH_3@$C_{24}H_{12}$-Mg, with NH_3@$C_{24}H_{12}$-Mg and PH_3@$C_{24}H_{12}$-Mg having the same energy gap value of 5.297 eV. In the water phase, the studied gases adsorbed on $C_{24}H_{12}$-Mg show a decreasing trend of 5.273 eV > 5.262 eV > 5.254 eV for AsH_3@$C_{24}H_{12}$-Mg, NH_3@$C_{24}H_{12}$-Mg and PH_3@$C_{24}H_{12}$-Mg, respectively. It is only in the water phase that the sensing of NH_3 on $C_{24}H_{12}$-Mg does not have the lowest energy gap value. The lowest energy gap values for the studied gases are observed in the water phase, while the highest are attributed to the gas phase. The different phases in which the adsorption process of AsH_3, NH_3 and PH_3 on $C_{24}H_{12}$-Mg were analyzed show an increasing trend in terms of the energy gap of water < ethanol < benzene < gas with values within the range of 5.2–6.4 eV. Hence, it can be deduced that since AsH_3@$C_{24}H_{12}$-Mg has the highest energy gap in all investigated phases, it has the most stable structure, since a higher energy gap corresponds to better stability of a structure. Depictions of the HOMO and LUMO plots are presented in Fig. 2. The HOMO and LUMO plots are similar in the different phases; hence, only the representation of the gas phase is presented in this paper. Furthermore, the HOMO and LUMO energy values can be used to obtain the quantum descriptors. These quantum descriptors include the ionization potential (IP), electron affinity (EA), electronegativity (χ), chemical potential (μ), chemical hardness (η), chemical softness (σ) and electrophilicity (ω). According to Koopmans' hypothesis, these quantum descriptors can be obtained from eqn (3)–(9).

$$\mathrm{IP} = -E_{\mathrm{HOMO}} \quad (3)$$

$$\mathrm{EA} = -E_{\mathrm{LUMO}} \quad (4)$$

$$\chi = 1/2(\mathrm{IP} + \mathrm{EA}) \quad (5)$$

$$\mu = -1/2(\mathrm{IP} + \mathrm{EA}) \quad (6)$$

$$\eta = 1/2(\mathrm{IP} - \mathrm{EA}) \quad (7)$$

$$\sigma = \frac{1}{2\eta} \quad (8)$$

$$\omega = \frac{\mu^2}{2\eta} \quad (9)$$

These quantum descriptors were studied to further authenticate the results explained by the energy gap. The ionization potential (IP) is the negative of the E_{HOMO} while the electron affinity (EA) is the negative of the E_{LUMO}.[59] The ionization potential (IP) and the chemical hardness (η) help to further determine the stability of the surfaces.[60] High energy values of the ionization potential (IP) and the chemical hardness (η) correspond to better stability of the surfaces being studied.[61,62] In all scenarios of the adsorption process of AsH_3, NH_3 and PH_3 on $C_{24}H_{12}$-Mg, high ionization potential (IP) and chemical hardness (η) values are observed, which further indicate the good stability properties of the surfaces.

3.3 Density of states

To gain further insight into the electronic properties and to visualize the change in the energy gap resulting from the XH_3 (X = As, N, P) gas adsorption on the magnesium-decorated graphene surface, the corresponding density of states (DOS) plots are presented in Fig. 3.[63] As shown in Fig. 3, the adsorption of XH_3 (X = As, N, P) in the gas phase results in new energy states appearing close to the Fermi energy level for the XH_3@$C_{24}H_{12}$-Mg (X = As, N, P) complexes. This led to the decrease in E_g from 6.331 eV ($C_{24}H_{12}$-Mg) to 6.313, 6.302, and 6.317 eV for the AsH_3@$C_{24}H_{12}$-Mg, NH_3@$C_{24}H_{12}$-Mg, and PH_3@$C_{24}H_{12}$-Mg complexes, respectively (see Table 2). The reduction in E_g indicates that the $C_{24}H_{12}$-Mg surface can detect the three gases.[64] However, comparing the total density of states (TDOS) plots in Fig. 3, the alteration of the TDOS plots is more pronounced in the NH_3@$C_{24}H_{12}$-Mg plot when compared with that of the

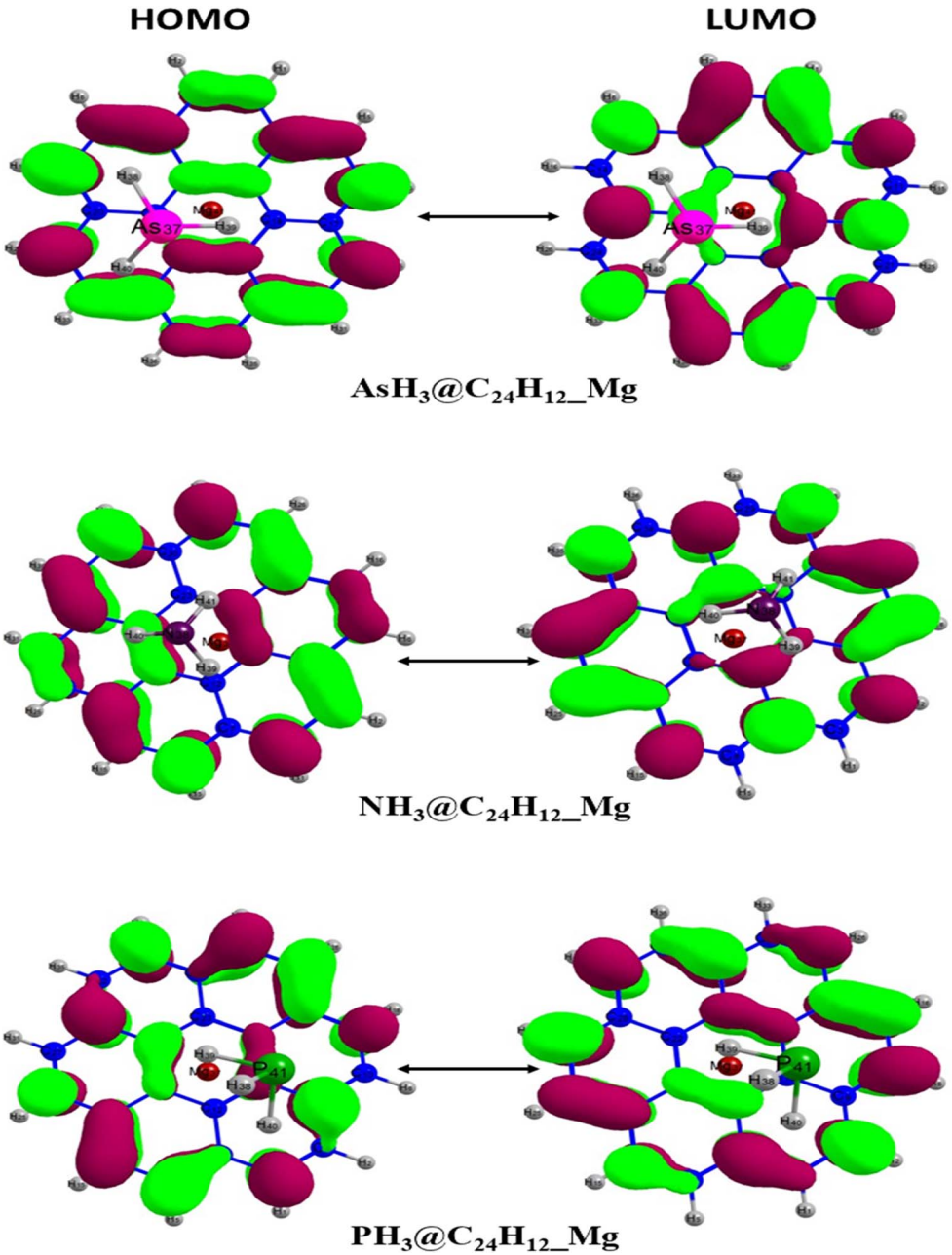

Fig. 2 Optimized HOMO and LUMO isosurface plots of AsH_3@$C_{24}H_{12}$-Mg, NH_3@$C_{24}H_{12}$-Mg and PH_3@$C_{24}H_{12}$-Mg.

magnesium-decorated graphene quantum dot surface, indicating that the $C_{24}H_{12}$-Mg surface has sensitivity for NH_3 gas.

3.4 Natural bond orbital (NBO) analysis

Natural bond orbital (NBO) analysis of the gas-adsorbed surface was undertaken in this study to chemically understand the distribution of the charges between the donor and acceptor orbitals.[65] In addition to investigating the charge distribution between orbitals, natural bond orbital analysis is a tool that explains the bond type and nature of bonding interactions, as well as intermolecular and intramolecular interaction.[66,67] The DFT method used earlier for evaluating the optimized structure was also employed in the NBO analysis. The nature of the interaction between the donor and the acceptor orbitals denoted by the stabilization energy is often referred to as the second-order perturbation energy, and it can be represented as eqn (10):

$$E^{(2)} = \Delta E_{ij} = q_i \left(\frac{(Fij)^2}{E(i) - E(j)} \right) \quad (10)$$

where q_i represents the donor occupancy, $F(i,j)$ is the off-diagonal NBO Fock Matrix elements, and E_i and E_j are the diagonal elements. Through literature reviews, it can be understood that when the values of the stabilization energy are large, it indicates the existence of a strong interaction between

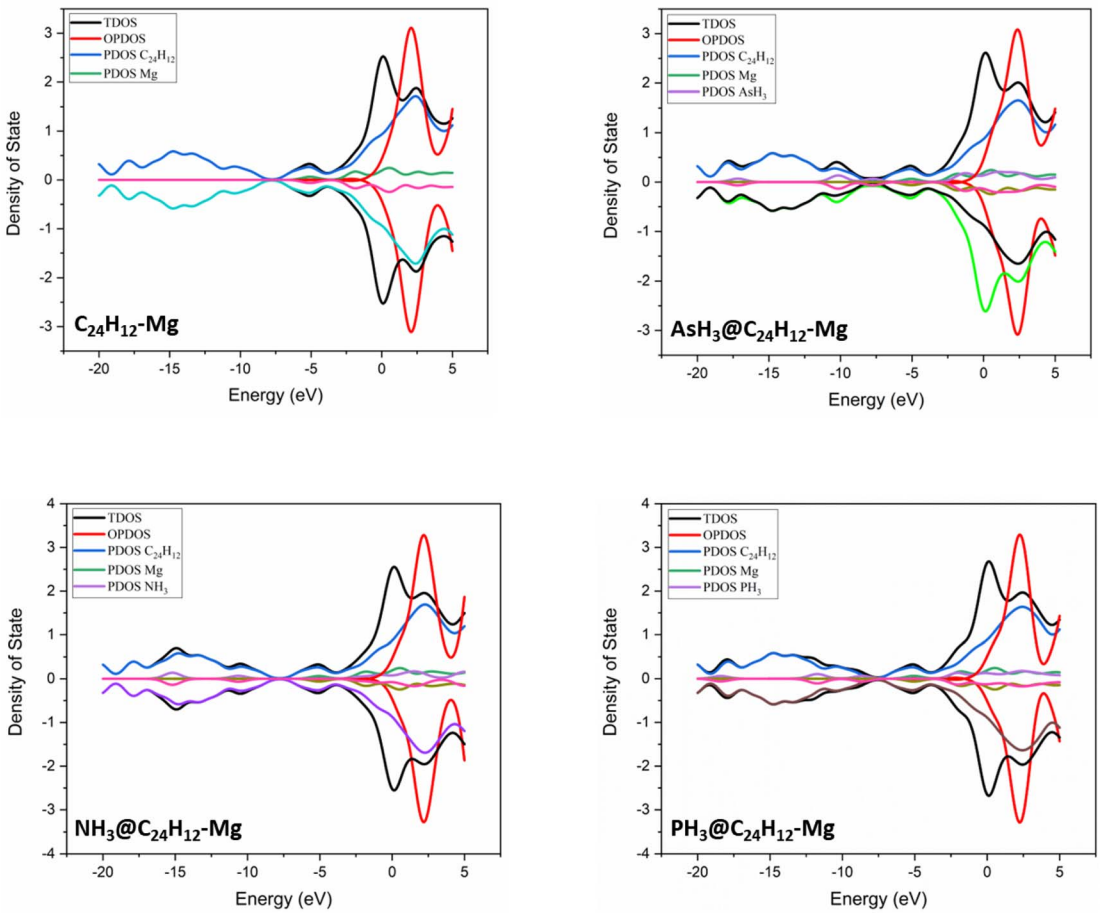

Fig. 3 Density of states plots for XH_3 (X = As, N, P) on the magnesium-decorated graphene quantum dot surface.

the donor and acceptor orbital.[68] It also indicates a higher degree of conjugation of the whole system under study.[69] In this paper, the estimated stabilization energy for the gas-adsorbed surfaces for the different phases have been computed and are tabulated in Table 3 alongside their respective donors (i), acceptors (j) and their diagonal elements with the off-diagonal NBO Fock Matrix elements. Close examination of Table 3 shows that the major transitions attributed to the system under study are BD (1) → BD* (1) which is the σ → σ* bond, BD (1) → BD* (2) [σ → π*], BD (2) → BD* (1) [π → σ*], BD (2) → BD* (2) [π → π*] and BD* (2) → BD* (1) [π* → σ*]. Other transitions observed in NBO analysis but not tabulated include the Rydberg (RY) and the center core pair (CR). The computed stabilization energies presented in Table 3 are in the range of 79–100 kcal mol^{-1}. From the displayed stabilization energies, in the gas phase, it can be observed that the gas-adsorbed surfaces follow the trend $AsH_3@C_{24}H_{12}$-Mg > $NH_3@C_{24}H_{12}$-Mg > $PH_3@C_{24}H_{12}$-Mg in terms of stabilization energy. Their values are 98.83 kcal mol^{-1}, 96.60 kcal mol^{-1} and 93.36 kcal mol^{-1}, respectively. In the benzene phase, the π → σ* transition is prominent. $AsH_3@C_{24}H_{12}$-Mg is observed to have higher values of second-order perturbation energy compared to the other gas-adsorbed surfaces. The other two phases, ethanol and water, also support the results obtained in the other phases. The values of the stabilization energy are similar to each other because of the similarly in the structure of the surfaces being studied. From the NBO analysis, it can also be noted that the σ → σ* transition contributed more to the stabilization of the gas-adsorbed surfaces.

3.5 Topological analysis – quantum theory of atoms-in-molecules (QTAIM)

Using the optimized $XH_3@C_{24}H_{12}$-Mg (X = As, N, P) structures, we carried out Bader's QTAIM analysis to investigate the bond type and inter- or intra-molecular nature of the interactions that exist between the interacting atoms of the XH_3 gases and the magnesium-decorated graphene quantum dot surface.[70] Based on QTAIM theory, the chemical bond existing between two interacting atoms is characterized by a topological (3, −1) point through-space known as the bond critical points (BCPs).[71] Topological parameters at the BCPs, such as the density of electrons $\rho(r)$, Laplacian electron density $\nabla^2\rho(r)$, Lagrangian kinetic energy $G(r)$, potential electron energy density $V(r)$, total electron energy density $H(r)$, Eigenvalues (λ_1, λ_2, λ_3), and the ellipticity ε are vital parameters in determining the nature of interactions.[72,73] The values of these parameters as calculated at the WB97XD/6-311++ (2d,2p) level of theory are presented in Table 4, and the corresponding QTAIM graph is shown in Fig. 4. The small values of electron

Table 3 Donors (*i*), acceptors (*j*), second-order perturbation energy and their diagonal elements with the off-diagonal NBO Fock matrix elements for the investigated surfaces calculated using the DFT/ωB97XD/6-311++G(2p,2d) method

Phase	System	Donor (*i*)	Acceptor (*j*)	$E(2)$ kcal mol^{-1}	$E(j) - E(i)$ a.u.	$F(i,j)$ a.u.
Gas	$AsH_3@C_{24}H_{12}$-Mg	σ (C_3–C_4)	π* (C_{10}–C_{14})	99.78	3.52	0.515
		σ (C_{17}–C_{21})	σ* (C_{12}–C_{18})	98.85	1.72	0.366
	$NH_3@C_{24}H_{12}$-Mg	σ (C_3–C_7)	σ* (C_9–C_{13})	97.72	0.68	0.230
		σ (C_{11}–C_{17})	σ* (C_{24}–H_{26})	97.94	0.91	0.267
	$PH_3@C_{24}H_{12}$-Mg	π* (C_{32}–C_{34})	σ* (C_{22}–C_{28})	84.98	1.41	0.895
		π* (C_9–C_{13})	σ* (C_{24}–C_{29})	95.48	0.51	0.208
Benzene	$AsH_3@C_{24}H_{12}$-Mg	σ (C_{17}–C_{21})	σ* (C_{30}–C_{34})	85.46	0.03	0.046
		π (C_{19}– C_{20})	σ* (C_4–C_9)	98.83	10.73	1.740
	$NH_3@C_{24}H_{12}$-Mg	σ (C_{19}– C_{20})	σ* (C_7–C_8)	83.05	0.39	0.160
		π (C_{19}– C_{20})	σ* (C_{17}–C_{21})	96.60	2.56	0.497
	$PH_3@C_{24}H_{12}$-Mg	π (C_8–C_{11})	π* (C_{19}–C_{20})	82.92	2.50	0.382
		π (C_8–C_{11})	σ* (C_{29}–C_{33})	93.36	4.11	0.586
Ethanol	$AsH_3@C_{24}H_{12}$-Mg	σ (C_3–C_4)	σ* (C_{30}–C_{34})	94.15	0.16	0.110
		σ (C_{21}–C_{27})	σ* (C_{30}–C_{34})	95.72	0.12	0.097
	$NH_3@C_{24}H_{12}$-Mg	σ (C_{19}–C_{23})	π* (C_{19}–C_{20})	92.62	1.69	0.392
		σ (C_{21}–C_{27})	π* (C_{19}–C_{20})	92.81	14.99	1.623
	$PH_3@C_{24}H_{12}$-Mg	π (C_8–C_{11})	π* (C_{19}–C_{20})	83.40	0.30	0.149
		σ (C_7–C_{12})	σ* (C_{19}–C_{20})	92.85	0.95	0.265
Water	$AsH_3@C_{24}H_{12}$-Mg	σ (H_2–C_4)	σ* (C_{20}–C_{24})	93.11	0.19	0.120
		σ (C_7–C_{12})	σ* (C_{20}–C_{24})	94.61	0.36	0.166
	$NH_3@C_{24}H_{12}$-Mg	π* (C_{10}–C_{14})	σ* (C_8–C_{11})	79.96	0.36	0.448
		σ (C_{27}–C_{28})	σ* (H_2–C_4)	93.98	0.40	0.174
	$PH_3@C_{24}H_{12}$-Mg	σ (H_6–C_{10})	σ* (C_{19}–C_{23})	89.36	0.75	0.232
		σ (C_7–C_{12})	σ* (C_{12}–C_{18})	93.75	0.93	0.265

Table 4 Study of weak interactions on the basis of bond critical point (BCP) and topological analysis parameters

System	Bond	$\rho(r)$	$\nabla^2(r)$	$G(r)$	$H(r)$	$V(r)$	$-G(r)/V(r)$	λ_1	λ_2	λ_3
$AsH_3@C_{24}H_{12}$-Mg	C_{12}–Mg_{41}	0.00061	0.00323	0.00055	0.00025	−0.00029	1.89655	−0.00023	−0.00003	0.00350
	C_{23}–As_{37}	0.00528	0.01586	0.00295	0.00100	−0.00195	1.51282	−0.00090	−0.00002	0.01678
$NH_3@C_{24}H_{12}$-Mg	C_{13}–Mg_{37}	0.00062	0.00326	0.00055	0.00026	−0.00029	1.89655	−0.00031	−0.00012	0.00370
	C_{19}–H_{41}	0.00406	0.01382	0.00263	0.00081	−0.00018	1.46111	−0.00214	−0.00092	0.01689
	C_{13}–N_{38}	0.00388	0.01362	0.00257	0.00083	−0.00173	1.48554	−0.00202	−0.00021	0.01585
	C_{22}–H_{40}	0.00372	0.01253	0.00239	0.00073	−0.00166	1.43975	−0.00203	−0.00080	0.01537
$PH_3@C_{24}H_{12}$-Mg	C_{22}–Mg_{37}	0.00059	0.00318	0.00053	0.00025	−0.00028	1.89285	−0.00018	−0.00007	0.00343
	C_{13}–Mg_{37}	0.00058	0.00317	0.00053	0.00025	−0.00028	1.89285	−0.00015	−0.00005	0.00338
	C_{13}–P_{41}	0.00564	0.01953	0.00371	0.00117	−0.00254	1.46063	−0.00143	−0.00072	0.02169

density with $\rho(r)$ < 0.1 a.u. signify non-covalent interaction between the XH_3 (X = As, N, P) gases and magnesium-decorated graphene quantum dot surface.[74] Also, positive values for the Laplacian electron density ($\nabla^2\rho(r) > 0$) and the total electron energy density ($H(r) > 0$) imply non-covalent interactions.[75] As shown in Table 4, the $\rho(r)$ values range between 0.00058 to 0.00564 a.u., whereas the $\nabla^2\rho(r)$ and $H(r)$ values range between 0.00025 to 0.01953 a.u. The $\rho(r)$ values are less than 0.1 a.u. and both the $\nabla^2\rho(r)$ and $H(r)$ values are positive for all interactions, which indicates the dominance of non-covalent forces between the interacting systems.[76] Furthermore, calculating the values of the ratio $-G(r)/V(r)$ gives further insight into the nature of the interactions.[77] As shown in Table 4, the $-G(r)/V(r)$ values of >1 for all studied interactions confirm the non-covalent nature of the interactions. From the discussion above, it is evident that the formation of the $XH_3@C_{24}H_{12}$-Mg (X = As, N, P) complexes occurs essentially through non-covalent interactions.

3.6 Noncovalent interactions (NCI)

The QTAIM analysis shows that non-covalent forces play the major role in the interactions between the XH_3 (X = As, N, P) gases and the magnesium-decorated graphene quantum dot surface. Therefore, it is important to further study the weak interactions using non-covalent interaction (NCI) analysis.[78] The NCI analysis is based on studying the plots of the reduced density gradient (RDG) against the product of the second Eigenvalue of the Hessian matrix (λ_2) with the electron density $\rho(\mathrm{sign}(\lambda_2)\rho)$.[79] Visualization of the weak interactions is carried out through 2D-RDG scatter maps and 3D iso-surface plots, which are presented in Fig. 5. The 2D-RDG scatter maps are interpreted using the peaks observed in the low-RDG and low-electron-density regions. The regions in which $\mathrm{sign}(\lambda_2)\rho$ < 0 indicates strong bonding, and $\mathrm{sign}(\lambda_2)\rho > 0$ indicates strong repulsive forces, whereas the point where $\mathrm{sign}(\lambda_2)\rho \approx$

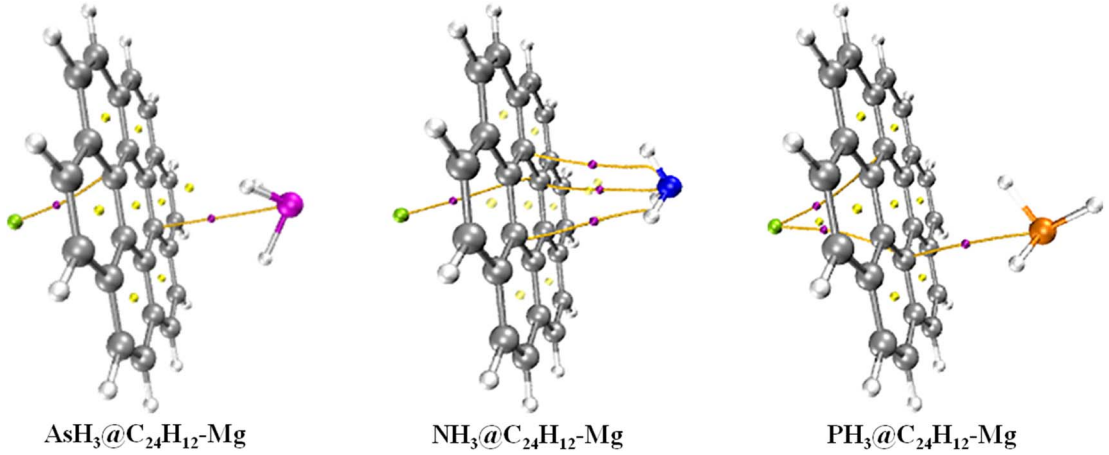

Fig. 4 Pictorial representation of the quantum theory of atoms-in-molecules (QTAIM) analysis.

0 indicates van der Waals (vdW) forces.[80] Similarly, NCI plots are interpreted using the blue-green-red color scale. Thus, the blue, green and red regions correspond to strong attraction, van der Waals (vdW), and steric repulsion forces, respectively.[81] From the 3D iso-surface plots in Fig. 5, green patches between the XH_3 (X = As, N, P) gases and the surface show that van der Waals (vdW) forces are the driving force for the adsorption of these gases onto the magnesium-decorated graphene quantum dot surface. Meanwhile, the red patches within the graphene surface result from repulsive steric effect from the rings forming the quantum dot structure. This was confirmed by the green and red spikes observable in the 2D-RDG scatter maps for all the studied $XH_3@C_{24}H_{12}$-Mg (X = As, N, P) complexes.

3.7 Adsorption study

In order to ensure a stable adsorption configuration, the structures were optimized separately before adsorption and optimized again upon adsorption. The cluster, initial structural equilibration has been carried out by employing the def2svp basis set. All calculations were carried out using the DFT/ωB97XD/6-311++G (2d,2p) method. To gain more insight into the effect of solvation on the adsorptive behavior of $C_{24}H_{12}$-Mg, calculations were carried out in four distinct phases: benzene, ethanol, water and gas. The adsorption behavior of the Mg-decorated graphene quantum dot ($C_{24}H_{12}$-Mg) surface in the adsorption of AsH_3, NH_3 and PH_3 was carried out using the calculation of adsorption energies of the respective complexes formed. Eqn (1) was employed in obtaining the different adsorption energies, and the results obtained are summarized in Table 5. Previous theoretical studies on the adsorption of gases agree that greater adsorption energy is favorable in comparative studies among different systems. That is, the greater the adsorption energy, the more likely that an adsorbent material best adsorbs the adsorbate under study.[82] From the data presented in Table 5, it is apparent that all the calculated adsorption energies are of a negative magnitude. Thus, this adsorption phenomenon is best described as chemisorption.[83] The adsorption energies can be arranged in an increasing trend of $NH_3@C_{24}H_{12}$-Mg < $PH_3@C_{24}H_{12}$-Mg < $AsH_3@C_{24}H_{12}$-Mg. This pattern was observed to apply for all phases under consideration. Among the considered phases, the best adsorption performance was noted in the gas phase due to its highest values of adsorption energy as compared to its studied counterparts in benzene, ethanol and water. The adsorption of AsH_3 on the magnesium-decorated graphene quantum dot ($C_{24}H_{12}$-Mg) corresponding to $AsH_3@C_{24}H_{12}$-Mg complex reflects the highest E_{ad} value of −1.87819, indicating that AsH_3 is better adsorbed on the $C_{24}H_{12}$-Mg surface than NH_3 or PH_3. In addition, NH_3 and PH_3 were adsorbed similarly on the Mg-decorated graphene quantum dot ($C_{24}H_{12}$-Mg), which is accounted for by their similar adsorption energies. The adsorption energy values obtained here were in agreement with previously reported literature.[84,85] However, $PH_3@C_{24}H_{12}$-Mg exhibits a relatively higher energy, indicating that the adsorption of PH_3 is more favored than that of NH_3. Hence, the studied Mg-decorated graphene quantum dot ($C_{24}H_{12}$-Mg) surface exhibits stronger adsorption potency for the AsH_3 gas molecule than its studied counterparts. The idea of deformation energy is used to provide a thorough explanation of a substrate's capacity to accommodate an adsorbate. According to a literature review, when a molecule adheres to a surface, it may result in energy-intensive surface deformation. The adsorption energy, which is the energy released or absorbed when a molecule is adsorbed onto a surface, can be impacted by this deformation energy. The total stability of the adsorbed state can be impacted by the magnitude of the deformation energy. For instance, the adsorption energy will be reduced and the adsorption may be less stable if the deformation energy is high. The adsorption may be more stable if the deformation energy is low, and *vice versa*.[85] Although energy can impact the effectiveness of materials used in a variety of applications, including catalysis, gas separation, and energy storage, it is essential for forecasting and optimizing adsorption processes. From the results presented in Table 5, it can be seen that the studied systems have higher deformation energy in the gas phase compared to in the other solvents, and these higher values can be explained based on solvent effects.

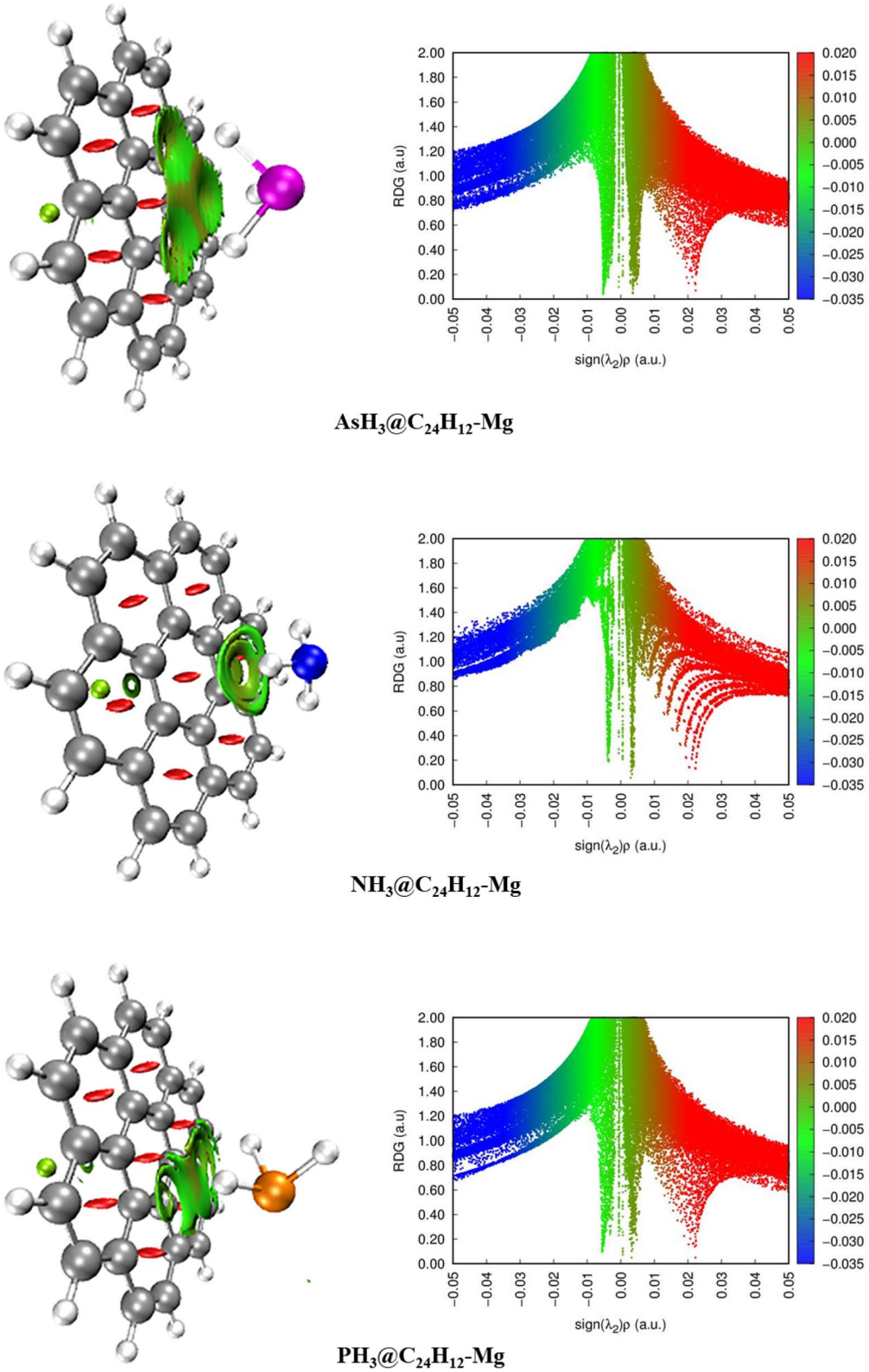

Fig. 5 Pictorial representation of the non-covalent interaction analysis.

3.8 Sensor mechanisms

The properties capable of describing the sensing performance of a material are generally regarded as sensor mechanisms. These mechanisms provide necessary insights from the interactions existing between the adsorbate and adsorbent materials through measuring the electrical conductivity, recovery time,

Table 5 Adsorption energies of the three studied systems in four distinct solvents: benzene, ethanol, water and gas, as calculated using the DFT/ωB97XD/6-311++G (2d, 2p) method

System	Benzene	Ethanol	Water	Gas
AsH_3@$C_{24}H_{12}$-Mg	−1.87601	−1.87192	−1.8737	−1.87819
NH_3@$C_{24}H_{12}$-Mg	−0.00641	−0.0056	−0.0056	−0.0067
PH_3@$C_{24}H_{12}$-Mg	−0.00755	−0.00746	−0.0075	−0.0076
Deformation energy				
AsH_3@$C_{24}H_{12}$-Mg	−2.312	−2.317	−2.315	−2.321
NH_3@$C_{24}H_{12}$-Mg	−2.123	−2.154	−2.165	−2.323
PH_3@$C_{24}H_{12}$-Mg	−2.212	−2.214	−2.132	−2.232

charge transfer, dipole moment and work function. These mechanisms have been theoretically explored in this section to strengthen the theoretical investigation of the adsorption of the three different gases on the Mg-decorated graphene quantum dot ($C_{24}H_{12}$-Mg).

3.8.1. Electrical conductivity. The ability of a molecule to conduct electricity can be attributed and traced to the flow of electrons between the HOMO and LUMO energies.[86] It is paramount to note that the energy gap is an essential parameter with the potential of predicting the electrical conductivity of a material. Therefore, it is safe to say that the reusability and stability of a material depend on the HOMO–LUMO energy gap. Previous theoretical studies have shown that electrical conductivity can be related to the energy gap in such a way that an increase in the energy gap induces a decrease in the conductivity of a material.[87] The inverse relationship in the conductivity can be demonstrated in eqn (11) as:

$$\sigma = AT^{2/3}e^{(E_g/2KT)} \quad (11)$$

where the electrical conductivity, Boltzmann constant, temperature and constant are denoted by σ, K, T and A, respectively. From the results obtained in Section 3.2 for the quantum descriptors, it is evident that NH_3@$C_{24}H_{12}$-Mg with the smallest energy gap possesses the lowest electrical conductivity. Furthermore, the relatively higher energy gap in PH_3@$C_{24}H_{12}$-Mg indicates the conducting nature of the material corresponding to the $C_{24}H_{12}$-Mg surface upon the adsorption of PH_3. Among the three gases, the highest conductivity was observed for the adsorption of AsH_3, and this is due to its high energy gap.

3.8.2. Recovery time and work function. One of the key parameters in investigating materials suitable for gas sensing is their reusability and stability.[88] The strength of an adsorption can be predicted by the interaction strength obtained from the adsorption energy, which is the chief parameter among other mechanisms.[89] The recovery time can be predicted from the adsorption energy using eqn (12).

$$\tau = \exp\left(-\frac{E_{ads}}{KT}\Big/\nu_0\right) \quad (12)$$

T, ν_0, K and E_{ad} are the temperature, attempted frequency, Boltzmann constant and adsorption energy, respectively. In the calculation, the Boltzmann constant can be approximated as $\sim 2.0 \times 10^{-3}$ kcal mol^{-1}, and the attempted frequency was obtained as 1.380649×10^{-23} m^2 kg s^{-2} K^{-1}.

To obtain the recovery time experimentally, the electric field and thermal effects are generally considered and utilized. Furthermore, the recovery time can be theoretically calculated from the transition state theory. In eqn (12), it can be noted that higher adsorption energy will increase the recovery time of a material, and thus, this concept is employed as follows. The adsorption follows an increasing trend of NH_3@$C_{24}H_{12}$-Mg < PH_3@$C_{24}H_{12}$-Mg < AsH_3@$C_{24}H_{12}$-Mg. From this trend, the order of increasing recovery time can likewise be illustrated. For example, the adsorption of AsH_3 on the surface reflects the greatest E_{ad} value of −1.87819. This implies that the AsH_3@$C_{24}H_{12}$-Mg system has the relatively longest recovery time.

The work function (φ), which is the minimum energy required to move the electron from the internal part of a solid to the surface, is an essential parameter in monitoring the electronic and optical characteristics of a material.[90] It is evident in Table 6 that the complexes resulting upon adsorption exhibited relatively more similar work function values of 3.3417, 3.4218 and 3.3284 eV for AsH_3@$C_{24}H_{12}$-Mg, NH_3@$C_{24}H_{12}$-Mg and PH_3@$C_{24}H_{12}$-Mg, respectively. It has been observed that the material indicated excellent adsorption potency in use for the adsorption of the gases.

3.8.3. Dipole moment and transfer. As one of the essential mechanisms of sensing, the dipole moment (μ_D) is used to gain insight into the charge separation of materials.[91] Necessary information on the dipole moment is important in tracking the interaction strength of studied systems. It is often seen that the quantity of charge transferred has a direct way of affecting the dipole moment.[92] The variability in the studied surface before and after the adsorption of AsH_3, NH_3 and PH_3 molecules is summarized in Table 6. Also, the effect of solvation on the adsorption of gases has been investigated from the perspective of the dipole moment. The dipole moment was calculated in benzene, ethanol, water and gas in order to investigate the adsorption behavior in the aforementioned solvents. Upon adsorption, higher dipole moments are observed in ethanol and water, with the dipole moments of 1.019102, 2.498643 and 1.075318 D in ethanol and 1.145908, 2.656500 and 1.175505 D in water for AsH_3@$C_{24}H_{12}$-Mg, NH_3@$C_{24}H_{12}$-Mg and PH_3@$C_{24}H_{12}$-Mg, respectively. In addition, relatively higher dipole moments are obtained in gas as compared to benzene. The greater dipole moments observed in these solvents are an indication of greater charge separation, which further implies strong interaction. The interactions in the four distinct solvents increase in the order benzene < gases < ethanol < water. A thorough literature search indicates that higher dipole moment is an indication of strong interactions.[93] Herein, NH_3@$C_{24}H_{12}$-Mg exhibits the highest dipole moment, followed by PH_3@$C_{24}H_{12}$-Mg. This indicates that NH_3@$C_{24}H_{12}$-Mg exhibits the strongest interaction in benzene and ethanol. However, a slight change in the behavior of adsorption was observed in gas, where the strongest interaction was noted for PH_3@$C_{24}H_{12}$-Mg as a result of its highest μ_D of 0.954942 D.

Table 6 Dipole moment (μ_D) in four distinct phases, and charge transfer (Q) and work function (φ) in gas calculated using the DFT/ωB97XD/6-311++G(2d,2p) method[a]

	Dipole moment				Charge transfer			
System	Benzene	Ethanol	Gas	Water	Q_C	Q_{ads}	Q_t	φ
$C_{24}H_{12}$-Mg	0.4283	0.9537	1.0203	0.5935	—	—	—	3.3605
AsH_3@$C_{24}H_{12}$-Mg	0.2106	1.0191	0.4231	1.1459	−0.0785	−1.1180	1.03945	3.3417
NH_3@$C_{24}H_{12}$-Mg	1.6430	2.4986	0.9091	2.6565	−0.1874	0.0162	−0.236	3.4218
PH_3@$C_{24}H_{12}$-Mg	0.6902	1.0753	0.9549	1.1755	0.0760	0.3343	−0.2584	3.3284

[a] Q_C and Q_{ads} are the respective charges on carbon and adsorbates.

Milliken charge analysis has been employed in tracing the charge transfer of the respective atoms present in the decorated $C_{24}H_{12}$ surface. The electronic charge transfer occurring between the two interacting compounds, such as the adsorbate and adsorbent, was investigated *via* the natural charge on the $C_{24}H_{12}$-Mg surface before and upon interaction, and the results are summarized in Table 6. Changes in charge transfer (Q_t) of 1.03945, −0.236 and −0.2584 are attributed to AsH_3@$C_{24}H_{12}$-Mg, NH_3@$C_{24}H_{12}$-Mg and PH_3@$C_{24}H_{12}$-Mg, respectively. From this, the strongest charge transfer was encountered in the adsorption of AsH_3 on the $C_{24}H_{12}$-Mg surface. This is evident in the AsH_3@$C_{24}H_{12}$-Mg system with the highest Q_t value. Furthermore, relatively strong charge transfer is noted in the PH_3@$C_{24}H_{12}$-Mg system, indicating strong charge transfer upon the adsorption of PH_3 on the Mg-decorated graphene quantum dot ($C_{24}H_{12}$-Mg).

3.9 Nonlinear optics (NLO) analysis

Nonlinear optics (NLO) studies the deflection of high-intensity lasers *via* interaction with a material.[94] A material is polarized when charged particles are dislodged within the material and a dipole moment is set up; on the other hand, static polarizabilities are utilized to investigate intramolecular and intermolecular interactions in a molecule.[95] It accurately predicts excited states in density functionals and represents the initial response of the electron density to electric fields. The primary goal of this objective is to conduct theoretical research on the complexes' optical properties. Strongly hyper-polarizable molecules, which have a wide range of technological applications, can be used to create NLO materials. Nonlinear optical materials have grown in prominence recently because of their prospective applications in fields such as laser technology, optical communication, optical data storage, and optical signal processing.[96] There are numerous optoelectronic and photonic applications for them as well. Organic chromophores may be a good substitute for inorganic materials because of their potent and rapid nonlinearities. This occurs as a result of their propensity to contribute to electron delocalization. Asymmetric polarization caused by electron donor and acceptor groups on each side of the molecule at the proper places in molecular systems is used to create effective organic materials for nonlinear optical effects.[97] The Gaussian 16 program was used to perform the calculations. The polarizabilities were calculated during the geometry optimization, and the NLO descriptors were generated using the coordinate values taken from the log file. Calculations of the frequency-dependent electronic hyperpolarizability and static polarizability, denoted by the symbols β_{xyz} and α_{xyz}, were made using the coupled-perturbed Hartree–Fock method. Calculation of the polarizabilities of molecules can be done using the basis set. The Multiwfn tool was used to calculate the NLO descriptors from the output of the Gaussian log file. The dipole moments (μ), polarizability anisotropies (α), isotropically averaged polarizabilities ($\Delta\alpha_{total}$), and isotopic first-order hyperpolarizabilities (β_{total}), which were calculated using eqn (13)–(19) below, were among the parameters obtained.

$$\mu = \sqrt{\mu^2 x + \mu^2 y + \mu^2 z}, \tag{13}$$

$$\langle\alpha\rangle = \frac{1}{3}(\alpha xx + \alpha yy + \alpha zz), \tag{14}$$

$$\Delta\alpha_{total} = \left\{\frac{1}{2}\left[(\alpha xx - \alpha yy)^2 + (\alpha xx - \alpha zz)^2 + (\alpha yy - \alpha zz)^2 + 6\left(\alpha^2 xy + \alpha^2 xz + \alpha^2 yz\right)\right]\right\}^{1/2}, \tag{15}$$

$$\beta_{total} = \sqrt{\beta^2 x + \beta^2 y + \beta^2 z}, \tag{16}$$

where,

$$\beta_x = \beta_{xxx} + \beta_{xyy} + \beta_{xzz} \tag{17}$$

$$\beta_y = \beta_{yyy} + \beta_{xxy} + \beta_{yzz} \tag{18}$$

$$\beta_z = \beta_{zzz} + \beta_{xzz} + \beta_{yyz} \tag{19}$$

The results predicted the dipole moment (μ), polarizability anisotropy $\langle\alpha\rangle$, average polarizability, isotopically averaged

Table 7 NLO descriptors of magnesium-decorated graphene quantum dot structure and interactions with the adsorbed gases calculated at DFT/ωB97XD/6-311++G(2p,2d) method

Structure	Dipole moment (μ)	Polarizability anisotropies (α_{total}) a.u.	Averaged polarizabilities $\langle\alpha\rangle$ a.u.	First-order hyperpolarizabilities (β_{total}) a.u.
$C_{24}H_{12}$-Mg	1.0202	47.85854359	−139.91287	67.98918423
NH_3@$C_{24}H_{12}$-Mg	0.9092	69.52853744	−150.27543	20.14768183
PH_3@$C_{24}H_{12}$-Mg	0.9549	46.91934464	−155.86527	75.39993366
AsH_3@$C_{24}H_{12}$-Mg	0.4231	44.1052877	−161.8569	237.4505579

polarizability ($\Delta\alpha_{total}$) and first-order hyperpolarizabilities (β_{total}) of the complexes. As presented in Table 7, the non-linear optic properties of $C_{24}H_{12}$-Mg, NH_3@$C_{24}H_{12}$-Mg, PH_3@$C_{24}H_{12}$-Mg and AsH_3@$C_{24}H_{12}$-Mg showed an increase in the dipole in the order $C_{24}H_{12}$-Mg: 1.0202μ > PH_3@$C_{24}H_{12}$-Mg: 0.9547μ > NH_3@$C_{24}H_{12}$-Mg: 0.9092μ > AsH_3@$C_{24}H_{12}$-Mg: 0.4231μ. The polarizability anisotropy increased in the order NH_3@$C_{24}H_{12}$-Mg: 69.528 > $C_{24}H_{12}$-Mg: 47.858 > PH_3@$C_{24}H_{12}$-Mg: 46.919 > AsH_3@$C_{24}H_{12}$-Mg: 44.105 a.u., and the averaged polarizability increased in the order $C_{24}H_{12}$-Mg: −139.912 > NH_3@$C_{24}H_{12}$-Mg: −150.275 > PH_3@$C_{24}H_{12}$-Mg: −155.865 > AsH_3@$C_{24}H_{12}$-Mg: −161.856 a.u., while the first-order hyperpolarizability increased in the order AsH_3@$C_{24}H_{12}$-Mg: 237.450 > PH_3@$C_{24}H_{12}$-Mg: 75.399 > $C_{24}H_{12}$-Mg: 67.989 > NH_3@$C_{24}H_{12}$-Mg: 20.147 a.u. The high first-order hyperpolarizability of AsH_3@$C_{24}H_{12}$-Mg makes it a suitable material for optoelectronic applications.

3.10 Thermodynamics properties

To fully understand the dynamics of heat and energy transfer present in the magnesium-decorated graphene quantum dot, as well as the spontaneity of the reaction involving graphene in sensing toxic gases like AsH_3, NH_3, and PH_3 in the surroundings, the thermodynamics properties were studied in the gas phase and in the solvents benzene, ethanol and water to enable us to ascertain the effects of the above-mentioned solvents on the thermodynamics of the sensor material.[98] The enthalpy (H) which is the sum total of a system's internal energy (Q) in addition to its constant pressure and total change in volume[99] $\Delta H = Q + p\Delta V$ was calculated for all the optimized studied complexes in both gas phase and solution using the equations below:

$$\Delta H^*\,(298\ \mathrm{K}) = \sum \Delta_f H^*\mathrm{product}\,(298\ \mathrm{K}) - \sum \Delta_f H^*\ \mathrm{reactants}\,(298\ \mathrm{K}) \quad (20)$$

$$\Delta_f H^*\,(298\ \mathrm{K}) = \sum (\varepsilon_0 + H_{corr})\ \mathrm{product} - \sum (\varepsilon_0 + H_{corr})\ \mathrm{reactants} \quad (21)$$

where ε_0 is the electronic energy and H_{corr} is sum of the electronic energy and thermal correction to H. To estimate the enthalpy of a system, the difference between the products and corresponding reactants should be obtained in order to ascertain whether the reaction is exothermic ($\Delta H > 0$) or endothermic ($\Delta H < 0$).[100] All the thermodynamic parameters are shown in Table 8. Also, detailed analysis of the thermodynamic calculations in different solvents has been presented in the ESI (Tables (1–3)†). As can be observed from the tabulated results, in the gas phase, which is the point of comparison, the reactions between the Mg-decorated graphene quantum dot were endothermic when interacting with NH_3 gas and exothermic when interacting with PH_3 and AsH_3. In the solvation-optimized structures in benzene, ethanol and water, all the interactions were noted to be exothermic; this is justified by the all-negative values of enthalpy of the systems that took part in the reaction. Similarly, the Gibbs free energy (ΔG) of a system undergoing a chemical reaction is described as the sum of the enthalpy and the product

Table 8 Thermodynamic parameters of the optimized structures, including the enthalpy and Gibbs free energy in the gas phase, calculated using the DFT/ωB97XD/6-311++G(2p,2d) method

Parameter	$C_{24}H_{12}$-Mg	AsH_3	AsH_3@$C_{24}H_{12}$-Mg	NH_3	NH_3@$C_{24}H_{12}$-Mg	PH_3	PH_3@$C_{24}H_{12}$-Mg
ε_0	−1121.867	−2237.627	−3359.566	−56.564	−1178.438	−343.150	−1465.025
ε_{ZPE}	0.283	0.021	0.306	0.035	0.318	0.024	0.308
E_{tot}	0.299	0.024	0.327	0.037	0.337	0.027	0.329
H_{corr}	0.300	0.025	0.328	0.038	0.338	0.028	0.330
G_{corr}	0.235	0.000	0.254	0.016	0.268	0.003	0.255
$\varepsilon_0 + \varepsilon_{ZPE}$	−1121.585	−2237.606	−3359.259	−56.530	−1178.120	−343.126	−1465.717
$\varepsilon_0 + E_{tot}$	−1121.568	−2237.603	−3359.239	−56.527	−1178.101	−343.123	−1465.696
$\varepsilon_0 + H_{corr}$	−1121.567	−2237.602	−3359.238	−56.526	−1178.100	−343.122	−1465.695
$\varepsilon_0 + G_{corr}$	−1121.632	−2237.627	−3359.312	−56.547	−1178.170	−343.147	−1465.770
$\Delta_f H^*$ (298 K)			−0.038		0.007		−1.081
$\Delta_f G^*$ (298 K)			−0.053		−0.009		−0.991

obtained from the summation of the system's temperature (K) and the entropy change (ΔS).[101] Thermodynamically, the Gibbs free energy of a system must be negative for a spontaneous reaction to occur, that is $\Delta G < 0$, while positive values of ΔG indicate non-spontaneity, that is, $\Delta G > 0$. The Gibbs free energy was calculated in this study using the equation below:[102]

$$\Delta_f G^*\ (298\ \mathrm{K}) = \sum(\varepsilon_0 + G_{\mathrm{corr}})\ \text{product} - \sum(\varepsilon_0 + G_{\mathrm{corr}})\ \text{reactants} \quad (22)$$

where ε_0 is the electronic energy and G_{corr} is the sum of electronic energy and the thermal correction to G. The results obtained in these comparative thermodynamic studies show that in the gaseous phase, all interactions of the Mg-decorated graphene quantum dot ($C_{24}H_{12}$-Mg) with the studied gases, namely, AsH_3, NH_3 and PH_3, were spontaneous in the order $NH_3@C_{24}H_{12}$-Mg > $AsH_3@C_{24}H_{12}$-Mg > $PH_3@C_{24}H_{12}$-Mg. In the benzene phase, $AsH_3@C_{24}H_{12}$-Mg and $PH_3@C_{24}H_{12}$-Mg were spontaneous, while $NH_3@C_{24}H_{12}$-Mg was non-spontaneous. In ethanol, $AsH_3@C_{24}H_{12}$-Mg and $NH_3@C_{24}H_{12}$-Mg were spontaneous in reaction, while $PH_3@C_{24}H_{12}$-Mg showed non-spontaneity. Finally, in water, the reaction between $AsH_3@C_{24}H_{12}$-Mg and $PH_3@C_{24}H_{12}$-Mg was spontaneous, whereas $NH_3@C_{24}H_{12}$-Mg was non-spontaneous. The results in all the studied phases suggest that the free energy of reaction in the studied systems for the formation of the product is most favorable for $AsH_3@C_{24}H_{12}$-Mg compared to other systems, and so the reaction of the Mg-decorated graphene quantum dot to sense AsH_3 gas will occur in a much easier and suitable state. These results are in agreement with the adsorption energy analysis as well as the HOMO–LUMO energy gap analysis as obtained in these studies.

4 Conclusions

Theoretical calculations were performed using the DFT/WB97XD/6-311++G(2p,2d) approach to investigate the selectivity, sensitivity, conductivity, and adsorption process of the graphene quantum dot and its decorated magnesium atom in sensing the hazardous hydride gases XH_3, where X = As, N, and P. This work was carried out in four different phases to comparatively study the effect of solvation and to deduce the best possible phase for the adsorption of the gases. From the structural properties, $PH_3@C_{24e}H_{12}$-Mg was observed to have the shortest bond length and $AsH_3@C_{24}H_{12}$-Mg to have the longest bond length in all phases. The bond lengths increased in the order $PH_3@C_{24}H_{12}$-Mg < $NH_3@C_{24}H_{12}$-Mg < $AsH_3@C_{24}H_{12}$-Mg. Comparing the four phases, the shortest bond length was found in the gas phase, while the longest was observed in the water phase. Upon adsorption of the gases on the magnesium-decorated graphene quantum dot, there was a slight reduction in the energy gaps, which enhances the conductivity and suggests the stability of the investigated surfaces. $AsH_3@C_{24}H_{12}$-Mg had the highest energy gap in all phases. The gas phase was observed to be the phase with the highest energy gap, followed by the benzene phase, the ethanol phase and finally the water phase. From the NBO analysis, the $\sigma \rightarrow \sigma^*$ transition contributed more to the stabilization of the gas-adsorbed surfaces. The interaction between the gas-adsorbed surfaces is a non-covalent interaction, as was confirmed through the QTAIM and NCI analyses. The nature of the adsorption is chemisorption, as indicated by the negative values of the adsorption energy. $AsH_3@C_{24}H_{12}$-Mg exhibited the highest adsorption energy, thus indicating that $AsH_3@C_{24}H_{12}$-Mg is best sensed on the magnesium-decorated graphene quantum dot. Based on our findings, the quantum dot under investigation has good sensing properties towards gases, and it has a higher sensing potency for the AsH_3 gas molecule than its examined counterparts. In comparison to the other phases, the gas phase is preferable.

Data availability

All data are contained within the manuscript and ESI.†

Author contributions

Ernest C. Agwamba and Hitler Louis: project conceptualization, design, and supervision. Praise O. Olagoke and Terkumbur E. Gber: writing, results extraction, analysis, and manuscript first draft. Gideon A. Okon: manuscript revision, review, and proofreading. Chidera F. Fedelis: manuscript proofreading. Adedapo S. Adeyinka: resources, review, and editing.

Conflicts of interest

All authors declare zero financial or inter-personal conflicts of interest that could have influenced the research work or results reported in this research paper.

Acknowledgements

This research was not funded by any Governmental or Non-governmental agency. The authors would like to acknowledge the centre for high performance computing (CHPC), at the University of Johannesburg, South Africa for providing computational resources for this research project.

References

1 S. Steinhauer, Gas sensors based on copper oxide nanomaterials: A review, *Chemosensors*, 2021, **9**(3), 51.
2 D. Lun and K. Xu, Recent Progress in Gas Sensor Based on Nanomaterials, *Micromachines*, 2022, **13**(6), 919.
3 F. Yin, W. Yue, Y. Li, S. Gao, C. Zhang, H. Kan and Y. Guo, Carbon-based nanomaterials for the detection of volatile organic compounds: A review, *Carbon*, 2021, **180**, 274–297.
4 N. Jamil, F. Jameel, S. Z. Bajwa, A. Rehman, R. F. H. Khan, A. Mahmood and W. S. Khan, Potential carbon nanotube–metal oxide hybrid nanostructures for gas-sensing applications, in *Metal Oxide-Carbon Hybrid Materials*, Elsevier, 2022, pp. 459–474.
5 R. Ahmad, S. M. Majhi, X. Zhang, T. M. Swager and K. N. Salama, Recent progress and perspectives of gas

sensors based on vertically oriented ZnO nanomaterials, *Adv. Colloid Interface Sci.*, 2019, **270**, 1–27.
6 N. M. Noah, Design and synthesis of nanostructured materials for sensor applications, *J. Nanomater.*, 2020, 1–20.
7 C. Hou, G. Tai, Y. Liu and X. Liu, Borophene gas sensor, *Nano Res.*, 2022, **15**(3), 2537–2544.
8 Y. Ghahramani, F. Fallahinezhad and M. Afsa, Graphene Quantum Dots and their applications: A mini-review, *Adv. Appl. NanoBio-Technol.*, 2021, 53–59.
9 R. K. Singh, R. Kumar, D. P. Singh, R. Savu and S. A. Moshkalev, Progress in microwave-assisted synthesis of quantum dots (graphene/carbon/semiconducting) for bioapplications: a review, *Mater. Today Chem.*, 2019, **12**, 282–314.
10 M. T. Hasan, R. Gonzalez-Rodriguez, C. Ryan, K. Pota, K. Green, J. L. Coffer and A. V. Naumov, Nitrogen-doped graphene quantum dots: Optical properties modification and photovoltaic applications, *Nano Res.*, 2019, **12**(5), 1041–1047.
11 T. K. Henna and K. Pramod, Graphene quantum dots redefine nanobiomedicine, *Mater. Sci. Eng., C*, 2020, **110**, 110651.
12 A. Ghaffarkhah, E. Hosseini, M. Kamkar, A. A. Sehat, S. Dordanihaghighi, A. Allahbakhsh and M. Arjmand, Synthesis, applications, and prospects of graphene quantum dots: a comprehensive review, *Small*, 2022, **18**(2), 2102683.
13 P. Kumar, C. Dhand, N. Dwivedi, S. Singh, R. Khan, S. Verma and A. K. Srivastava, Graphene quantum dots: A contemporary perspective on scope, opportunities, and sustainability, *Renewable Sustainable Energy Rev.*, 2022, **157**, 111993.
14 M. Li, T. Chen, J. J. Gooding and J. Liu, Review of carbon and graphene quantum dots for sensing, *ACS Sens.*, 2019, **4**(7), 1732–1748.
15 Y. R. Kumar, K. Deshmukh, K. K. Sadasivuni and S. K. Pasha, Graphene quantum dot based materials for sensing, bio-imaging and energy storage applications: a review, *RSC Adv.*, 2020, **10**(40), 23861–23898.
16 Q. He, B. Yu, Z. Li and Y. Zhao, Density functional theory for battery materials, *Energy Environ. Mater.*, 2019, **2**(4), 264–279.
17 P. Verma and D. G. Truhlar, Status and challenges of density functional theory, *Trends Chem.*, 2020, **2**(4), 302–318.
18 Q. Wang, Y. Zhou, X. Zhao, K. Chen, G. Bingni, T. Yang and J. Chen, Tailoring carbon nanomaterials *via* a molecular scissor, *Nano Today*, 2021, **36**, 101033.
19 T. E. Gber, H. Louis, A. E. Owen, B. E. Etinwa, I. Benjamin, F. C. Asogwa and E. A. Eno, Heteroatoms (Si, B, N, and P) doped 2D monolayer MoS 2 for NH 3 gas detection, *RSC Adv.*, 2022, **12**(40), 25992–26010.
20 Z. Li, L. Jia, J. Chen, X. Cui, W. Zeng and Q. Zhou, Ag-modified hexagonal GaN monolayer as an innovative gas detector toward SF6 decomposed species: Insights from the first-principles computations, *Appl. Surf. Sci.*, 2022, **589**, 153000.
21 A. Kumar, N. Sharma, A. P. Gutal, D. Kumar, P. Kumar, M. Paranjothy and M. Kumar, Growth and NO2 gas sensing mechanisms of vertically aligned 2D SnS2 flakes by CVD: Experimental and DFT studies, *Sens. Actuators, B*, 2022, **353**, 131078.
22 A. Nematollahzadeh, H. Basharnavaz, A. Habibi-Yangjeh, and S. H. Kamali, *Enhancing AsH3 Gas Adsorption*, 2021.
23 A. Nematollahzadeh, H. Basharnavaz, A. Habibi-Yangjeh and S. H. Kamali, Enhancing AsH3 Gas Adsorption Potentials of Graphitic Carbon Nitride by Codoping Cr/P, Mo/P, and W/P Atoms: A DFT Investigation, *J. Nanostructures*, 2021, **11**(4), 638–646.
24 A. Vouzavalis, *Fabrication And Characterization Of Electrochemical Ammonia Sensors*, Doctoral dissertation, University of Thessaly, 2018.
25 S. V. T. Coalition, *Toward a just and sustainable solar energy industry*, San Jose, 400, 2009.
26 A. T. M. Mustafa Kamal, *Occurrence and Characterization of Atmospheric Trace Gases in Dhaka City, Bangladesh*, Doctoral dissertation, University of Dhaka, 2018.
27 D. Penalva Milagro, *Chemical sensing of dangerous gases based on a 4G drone platform*, Bachelor's thesis, Universitat Politècnica de Catalunya, 2022.
28 V. A. Ranea, P. L. D. Quiña and N. M. Yalet, General adsorption model for H2S, H2Se, H2Te, NH3, PH3, AsH3 and SbH3 on the V2O5 (0 0 1) surface including the van der Waals interaction, *Chem. Phys. Lett.*, 2019, **720**, 58–63.
29 C. Winder, Toxicity of gases, vapours and particulates, in *Occupational toxicology*, CRC Press, 2004, pp. 399–424.
30 V. Vincent, The Place of Gas Analysis in Forensic Toxicology, *J. Forensic Leg. Investig. Sci.*, 2015, **1**(005), DOI: 10.24966/flis-733x/100005.
31 S. Singsen, N. Thatsami, P. Tangpakonsab, H. Bae, H. Lee, T. Hussain and T. Kaewmaraya, Transition-Metals Graphdiyne Monolayer as Efficient Sensor toward Phosphide (PH3) and Arsine (AsH3), *Phys. Chem. Chem. Phys.*, 2022, 26622–26630.
32 H. Luo, L. Zhang, S. Xu, M. Shi, W. Wu and K. Zhang, NH3, PH3 and AsH3 adsorption on alkaline earth metal (Be-Sr) doped graphenes: Insights from DFT calculations, *Appl. Surf. Sci.*, 2021, **537**, 147542.
33 H. Luo, K. Xu, Z. Gong, N. Li, K. Zhang and W. Wu, NH3, PH3, AsH3 adsorption and sensing on rare earth metal doped graphene: DFT insights, *Appl. Surf. Sci.*, 2021, **566**, 150390.
34 P. Buasaeng, W. Rakrai, B. Wanno and C. Tabtimsai, DFT investigation of NH3, PH3, and AsH3 adsorptions on Sc-, Ti-, V-, and Cr-doped single-walled carbon nanotubes, *Appl. Surf. Sci.*, 2017, **400**, 506–514.
35 R. Dennington, T. A. Keith and J. M. Millam, *GaussView, 6.0.16*, Semichem Inc., Shawnee Mission, KS, USA, 2001; T. HyperChem, HyperChem, 8.07, *HyperChem Professional Program*, Gainesville, Hypercube, 2016.
36 M. J. Frisch, G. W. Trucks, H. B. Schlegel, G. E. Scuseria, M. A. Robb, J. R. Cheeseman, G. Scalmani, V. Barone, G. A. Petersson, H. Nakatsuji, X. Li, M. Caricato, A. V. Marenich, J. Bloino, B. G. Janesko, R. Gomperts,

B. Mennucci, H. P. Hratchian, J. V. Ortiz, A. F. Izmaylov, J. L. Sonnenberg, D. Williams-Young, F. Ding, F. Lipparini, F. Egidi, J. Goings, B. Peng, A. Petrone, T. Henderson, D. Ranasinghe, V. G. Zakrzewski, J. Gao, N. Rega, G. Zheng, W. Liang, M. Hada, M. Ehara, K. Toyota, R. Fukuda, J. Hasegawa, M. Ishida, T. Nakajima, Y. Honda, O. Kitao, H. Nakai, T. Vreven, K. Throssell, J. A. Montgomery Jr, J. E. Peralta, F. Ogliaro, M. J. Bearpark, J. J. Heyd, E. N. Brothers, K. N. Kudin, V. N. Staroverov, T. A. Keith, R. Kobayashi, J. Normand, K. Raghavachari, A. P. Rendell, J. C. Burant, S. S. Iyengar, J. Tomasi, M. Cossi, J. M. Millam, M. Klene, C. Adamo, R. Cammi, J. W. Ochterski, R. L. Martin, K. Morokuma, O. Farkas, J. B. Foresman and D. J. Fox, *Gaussian 16, Revision C.01*, Gaussian, Inc., Wallingford CT, 2016.

37 R. Conte, P. L. Houston, C. Qu, J. Li and J. M. Bowman, Full-dimensional, *ab initio* potential energy surface for glycine with characterization of stationary points and zero-point energy calculations by means of diffusion Monte Carlo and semiclassical dynamics, *J. Chem. Phys.*, 2020, **153**(24), 244301.

38 M. K. Hema, C. S. Karthik, K. J. Pampa, P. Mallu and N. K. Lokanath, Solvent induced mononuclear and dinuclear mixed ligand Cu (II) complex: structural diversity, supramolecular packing polymorphism and molecular docking studies, *New J. Chem.*, 2020, **44**(41), 18048–18068.

39 G. A. Zhurko and D. A. Zhurko, *Chemcraft, Version 1.7 (Build 132)*, **http://www.chemcraftprog.com/**.

40 *Origin(Pro), Version 2018*, OriginLab Corporation, Northampton, MA, USA.

41 F. Weinhold, The Path to Natural Bond Orbitals, *Isr. J. Chem.*, 2022, **62**(1–2), e202100026.

42 T. Lu and F. Chen, Multiwfn: a multifunctional wavefunction analyzer, *J. Comput. Chem.*, 2012, **33**, 580–592.

43 W. Humphrey, A. Dalke and K. Schulten, VMD: visual molecular dynamics, *J. Mol. Graph.*, 1996, **14**, 33–38.

44 S. Shittu, G. Li, X. Zhao and X. Ma, Review of thermoelectric geometry and structure optimization for performance enhancement, *Appl. Energy*, 2020, **268**, 115075.

45 R. Rabeya, S. Mahalingam, A. Manap, M. Satgunam, M. Akhtaruzzaman and C. H. Chia, Structural defects in graphene quantum dots: A review, *Int. J. Quantum Chem.*, 2022, **122**(12), e26900.

46 G. Chen, L. Gan, H. Xiong and H. Zhang, Density functional theory study of B, N, and Si doped penta-graphene as the potential gas sensors for NH3 detection, *Membranes*, 2022, **12**(1), 77.

47 A. N. Sosa, J. E. Santana, Á. Miranda, L. A. Pérez, A. Trejo, F. Salazar and M. Cruz-Irisson, NH3 capture and detection by metal-decorated germanene: a DFT study, *J. Mater. Sci.*, 2022, **57**(18), 8516–8529.

48 B. J. Cid, J. E. Santana, L. G. Arellano, Á. Miranda, S. E. Pérez-Figueroa, M. I. Iturrios and M. Cruz-Irisson, Metal-decorated siligene as work function type sensor for NH3 detection: A DFT approach, *Appl. Surf. Sci.*, 2023, **610**, 155541.

49 E. Salih and A. I. Ayesh, First principle investigation of H2Se, H2Te and PH3 sensing based on graphene oxide, *Phys. Lett. A*, 2020, **384**(29), 126775.

50 E. A. Eno, F. A. Patrick-Inezi, H. Louis, T. E. Gber, T. O. Unimuke, E. C. Agwamba and S. A. Adalikwu, Theoretical investigation and antineoplastic potential of Zn (II) and Pd (II) Complexes of 6-Methylpyridine-2-carbaldehyde-N (4)-ethylthiosemicarbazone, *Chem. Phys. Impact*, 2022, **5**, 100094.

51 Q. S. Obu, H. Louis, J. O. Odey, I. J. Eko, S. Abdullahi, T. N. Ntui and O. E. Offiong, Synthesis, spectra (FT-IR, NMR) investigations, DFT study, *in silico* ADMET and Molecular docking analysis of 2-amino-4-(4-aminophenyl) thiophene-3-carbonitrile as a potential anti-tubercular agent, *J. Mol. Struct.*, 2021, **1244**, 130880.

52 H. Louis, T. E. Gber, F. C. Asogwa, E. A. Eno, T. O. Unimuke, V. M. Bassey and B. I. Ita, Understanding the lithiation mechanisms of pyrenetetrone-based carbonyl compound as cathode material for lithium-ion battery: Insight from first principle density functional theory, *Mater. Chem. Phys.*, 2022, **278**, 125518.

53 D. M. Mamand and H. M. Qadr, Density Functional Theory and Computational Simulation of the Molecular Structure on Corrosion of Carbon Steel in Acidic Media of Some Amino Acids, *Russ. J. Phys. Chem. A*, 2022, **96**(10), 2155–2165.

54 H. O. Edet, H. Louis, I. Benjamin, M. Gideon, T. O. Unimuke, S. A. Adalikwu and A. S. Adeyinka, Hydrogen storage capacity of C12X12 (X= N, P, and Si), *Chem. Phys. Impact*, 2022, **5**, 100107.

55 H. Louis, I. O. Amodu, T. O. Unimuke, T. E. Gber, B. B. Isang and A. S. Adeyinka, Modeling of Ca12O12, Mg12O12, and Al12N12 nanostructured materials as sensors for phosgene (Cl2CO), *Mater. Today Commun.*, 2022, **32**, 103946.

56 H. Louis, D. Etiese, T. O. Unimuke, A. E. Owen, A. O. Rajee, T. E. Gber and E. N. Nfor, Computational design and molecular modeling of the interaction of nicotinic acid hydrazide nickel-based complexes with H 2 S gas, *RSC Adv.*, 2022, **12**(47), 30365–30380.

57 M. D. Mohammadi, H. Y. Abdullah, H. Louis and G. E. Mathias, 2D Boron Nitride Material as a sensor for H2SiCl2, *Comput. Theor. Chem.*, 2022, 113742.

58 H. Louis, G. E. Mathias, O. J. Ikenyirimba, T. O. Unimuke, D. Etiese and A. S. Adeyinka, Metal-doped Al12N12X (X= Na, Mg, K) nanoclusters as nanosensors for carboplatin: insight from first-principles computation, *J. Phys. Chem. B*, 2022, **126**(27), 5066–5080.

59 M. D. Mohammadi, F. Abbas, H. Louis, G. E. Mathias and T. O. Unimuke, Trapping of CO, CO2, H2S, NH3, NO, NO2, and SO2 by polyoxometalate compound, *Comput. Theor. Chem.*, 2022, **1215**, 113826.

60 H. Louis, T. C. Egemonye, T. O. Unimuke, B. E. Inah, H. O. Edet, E. A. Eno and A. S. Adeyinka, Detection of Carbon, Sulfur, and Nitrogen Dioxide Pollutants with a 2D Ca12O12 Nanostructured Material, *ACS Omega*, 2022, **7**(39), 34929–34943.

61 H. Louis, D. E. Charlie, I. O. Amodu, I. Benjamin, T. E. Gber, E. C. Agwamba and A. S. Adeyinka, Probing the reactions of thiourea (CH4N2S) with metals (X= Au, Hf, Hg, Ir, Os, W, Pt, and Re) anchored on fullerene surfaces (C59X), *ACS Omega*, 2022, **7**(39), 35118–35135.

62 R. Hussain, M. Saeed, M. Y. Mehboob, S. U. Khan, M. U. Khan, M. Adnan and K. Ayub, Density functional theory study of palladium cluster adsorption on a graphene support, *RSC Adv.*, 2020, **10**(35), 20595–20607.

63 J. A. Agwupuye, H. Louis, T. O. Unimuke, P. David, E. I. Ubana and Y. L. Moshood, Electronic structure investigation of the stability, reactivity, NBO analysis, thermodynamics, and the nature of the interactions in methyl-substituted imidazolium-based ionic liquids, *J. Mol. Liq.*, 2021, **337**, 116458.

64 V. Nagarajan and R. Chandiramouli, Detection of trace level of hazardous phosgene gas on antimonene nanotube based on first-principles method, *J. Mol. Graphics Modell.*, 2019, **88**, 32–40.

65 H. Louis, O. J. Ikenyirimba, T. O. Unimuke, G. E. Mathias, T. E. Gber and A. S. Adeyinka, Electrocatalytic activity of metal encapsulated, doped, and engineered fullerene-based nanostructured materials towards hydrogen evolution reaction, *Sci. Rep.*, 2022, **12**(1), 1–21.

66 E. Nemati-Kande, R. Karimian, V. Goodarzi and E. Ghazizadeh, Feasibility of pristine, Al-doped and Ga-doped Boron Nitride nanotubes for detecting SF4 gas: A DFT, NBO and QTAIM investigation, *Appl. Surf. Sci.*, 2020, **510**, 145490.

67 W. Emori, G. J. Ogunwale, H. Louis, E. C. Agwamba, K. Wei, T. O. Unimuke, C. Cheng, E. U. Ejiofor, F. C. Asogwa and A. S. Adeyinka, Spectroscopic (UV-vis, FT-IR, FT-Raman, and NMR) analysis, structural benchmarking, molecular properties, and the in-silico cerebral anti-ischemic activity of 2 amino-6-ethoxybenzothiazole, *J. Mol. Struct.*, 2022, 133318.

68 M. Doust Mohammadi and H. Y. Abdullah, The adsorption of chlorofluoromethane on pristine, and Al-and Ga-doped boron nitride nanosheets: a DFT, NBO, and QTAIM study, *J. Mol. Model.*, 2020, **26**(10), 1–15.

69 W. Abisha, D. A. Dhas, S. Balachandran and I. H. Joe, Molecular Structure, Spectroscopic Elucidation (FT-IR, FT-Raman, UV-visible and NMR) with NBO, ELF, LOL, RDG, Fukui, Drug Likeness and Molecular Docking Analysis on Dimethomorph, *Polycyclic Aromat. Compd.*, 2022, 1–44.

70 E. A. Eno, J. I. Mbonu, H. Louis, F. S. Patrick-Inezi, T. E. Gber, T. O. Unimuke and O. E. Offiong, Antimicrobial activities of 1-phenyl-3-methyl-4-trichloroacetyl-pyrazolone: Experimental, DFT studies, and molecular docking investigation, *J. Indian Chem. Soc.*, 2022, **99**(7), 100524.

71 C. H. Suresh, G. S. Remya and P. K. Anjalikrishna, *Molecular electrostatic potential analysis: A powerful tool to interpret and predict chemical reactivity*, Wiley Interdisciplinary Reviews: Computational Molecular Science, 2022, p. e1601.

72 O. V. Rudnitskaya, T. A. Tereshina, E. V. Dobrokhotova, E. K. Kultyshkina, A. S. Novikov, A. G. Tskhovrebov and V. N. Khrustalev, Monoprotonated Dimethyl Sulfoxide,[HOSMe2]+: Synthesis, Crystal Structure, Spectroscopic and Theoretical Studies of [HOSMe2] 2 [OsCl6]·2H2O, *ChemistrySelect*, 2021, **6**(21), 5211–5217.

73 A. G. Tskhovrebov, A. S. Novikov, A. S. Kritchenkov, V. N. Khrustalev and M. Haukka, Attractive halogen halogen interactions in crystal structure of trans-dibromogold (III) complex, *Z. Kristallogr. Cryst. Mater.*, 2020, **235**(10), 477–480.

74 D. K. Miller, I. Y. Chernyshov, Y. V. Torubaev and S. V. Rosokha, From weak to strong interactions: structural and electron topology analysis of the continuum from the supramolecular chalcogen bonding to covalent bonds, *Phys. Chem. Chem. Phys.*, 2022, **24**(14), 8251–8259.

75 N. Kumar, S. Saha and G. N. Sastry, Towards developing a criterion to characterize non-covalent bonds: a quantum mechanical study, *Phys. Chem. Chem. Phys.*, 2021, **23**(14), 8478–8488.

76 M. Doust Mohammadi and H. Y. Abdullah, Non-covalent interactions of Cysteine onto C60, C59Si, and C59Ge: A DFT study, *J. Mol. Model.*, 2021, **27**(11), 1–14.

77 G. J. Ogunwale, H. Louis, T. E. Gber and A. S. Adeyinka, Modeling of pristine, Ir-and Au-decorated C60 fullerenes as sensors for detection of Hydroxyurea and Nitrosourea drugs, *J. Environ. Chem. Eng.*, 2022, 108802.

78 T. N. Lohith, M. K. Hema, C. S. Karthik, S. Sandeep, L. Mallesha, N. S. Alsaiari and S. R. Kumaraswamy, Persistent prevalence of non-covalent interaction in pyrimidine containing sulfonamide derivative: A quantum computational analysis, *J. Mol. Struct.*, 2022, 133378.

79 A. G. Tskhovrebov, A. S. Novikov, B. S. Tupertsev, A. A. Nazarov, A. A. Antonets, A. A. Astafiev and V. N. Khrustalev, Azoimidazole gold (III) complexes: Synthesis, structural characterization and self-assembly in the solid state, *Inorg. Chim. Acta*, 2021, **522**, 120373.

80 H. Li, J. Guo, Y. Zhang, L. Zhao, J. Gao and C. Xu, Research on separation of aromatics from FCC diesel using organic solvent: A combination of experiments and quantum chemical calculations, *Fuel*, 2022, **308**, 121982.

81 P. Peng, N. Ding, C. Zhao, Y. Li, J. Liu, S. Li and S. Pang, Improving the Stability of All-Carbon-Nitrated Azoles through Cocrystallization, *Cryst. Growth Des.*, 2022, **22**(4), 2158–2167.

82 A. H. Birniwa, A. S. Abubakar, H. N. M. E. Mahmud, S. R. M. Kutty, A. H. Jagaba, S. S. A. Abdullahi and Z. U. Zango, Application of agricultural wastes for cationic dyes removal from wastewater, in *Textile Wastewater Treatment*, Springer, Singapore, 2022, pp. 239–274.

83 H. Louis, O. J. Ikenyirimba, T. O. Unimuke, G. E. Mathias, T. E. Gber and A. S. Adeyinka, Electrocatalytic activity of metal encapsulated, doped, and engineered fullerene-based nanostructured materials towards hydrogen evolution reaction, *Sci. Rep.*, 2022, **12**(1), 1–21.

84 H. Luo, K. Xu, Z. Gong, N. Li, K. Zhang and W. Wu, NH3, PH3, AsH3 adsorption and sensing on rare earth metal

doped graphene: DFT insights, *Appl. Surf. Sci.*, 2021, **566**, 150390.

85 S. Singsen, N. Thasami, P. Tangpakonsab, H. Bae, H. Lee, T. Hussain and T. Kaewmaraya, Transition-metal decorated graphdiyne monolayer as an efficient sensor toward phosphide (PH 3) and arsine (AsH 3), *Phys. Chem. Chem. Phys.*, 2022, **24**(43), 26622–26630.

86 C. G. Apebende, H. Louis, A. E. Owen, I. Benjamin, I. O. Amodu, T. E. Gber and F. C. Asogwa, Adsorption properties of metal functionalized fullerene (C59Au, C59Hf, C59Ag, and C59Ir) nanoclusters for application as a biosensor for hydroxyurea (HXU): insight from theoretical computation, *Z. Phys. Chem.*, 2022, **236**(11–12), 1515–1546.

87 R. Dong, *Synthesis of Asymmetric Heterocycle-Fused Indacenes for Organic Electronic Application*, Doctoral dissertation, University of Oregon, 2022, **https://scholarsbank.uoregon.edu/xmlui/handle/1794/27512**.

88 R. Woods-Robinson, Y. Han, H. Zhang, T. Ablekim, I. Khan, K. A. Persson and A. Zakutayev, Wide band gap chalcogenide semiconductors, *Chem. Rev.*, 2020, **120**(9), 4007–4055.

89 M. V. Nikolic, V. Milovanovic, Z. Z. Vasiljevic and Z. Stamenkovic, Semiconductor gas sensors: Materials, technology, design, and application, *Sensors*, 2020, **20**(22), 6694.

90 M. Rakhshi, M. Mohsennia and H. Rasa, DFT Study of PH 3 Physisorption and Chemisorption on Boron Nitride Nanotubes, *Russ. J. Phys. Chem. A*, 2018, **92**, 540–546.

91 S. Sardarzadeh, J. Karamdel and P. Nayebi, Adsorption of SO2, H2S, NH3, PH3, and AsH3 Gas Molecules on Pristine Armchair Phosphorene Nanoribbon: A First-Principles Study, *Phys. Status Solidi B*, 2020, **257**(9), 2000120.

92 M. Chauhan, R. Kashyap, M. Singh, B. C. Choudhary and R. K. Sharma, A DFT Modulated Analysis of Manganese doped Graphene Nanoribbons as a potential material for sensing of highly toxic gases CO, PH3 and SbH3, *Phys. Scr.*, 2023, 045803.

93 J. Luo, D. Yu, K. D. Hristovski, K. Fu, Y. Shen, P. Westerhoff and J. C. Crittenden, Critical review of advances in engineering nanomaterial adsorbents for metal removal and recovery from water: Mechanism identification and engineering design, *Environ. Sci. Technol.*, 2021, **55**(8), 4287–4304.

94 P. Jiménez-Calvo, V. Caps and V. Keller, Plasmonic Au-based junctions onto TiO2, gC3N4, and TiO2-gC3N4 systems for photocatalytic hydrogen production: Fundamentals and challenges, *Renewable Sustainable Energy Rev.*, 2021, **149**, 111095.

95 D. Cortes-Arriagada, and D. E. Ortega, *Phosphorene–Fullerene nanostructures: A first-principles study*, 2021.

96 M. Veit, D. M. Wilkins, Y. Yang, R. A. DiStasio Jr and M. Ceriotti, Predicting molecular dipole moments by combining atomic partial charges and atomic dipoles, *J. Chem. Phys.*, 2020, **153**(2), 024113.

97 E. V. Kulakov, C. J. Sprain, P. V. Doubrovine, A. V. Smirnov, G. A. Paterson, L. Hawkins and A. J. Biggin, Analysis of an updated paleointensity database (QPI-PINT) for 65–200 Ma: Implications for the long-term history of dipole moment through the Mesozoic, *J. Geophys. Res.: Solid Earth*, 2019, **124**(10), 9999–10022.

98 S. Ravi, R. Sreedharan, K. R. Raghi, T. M. Kumar and K. Naseema, Linear–nonlinear optical and quantum chemical studies on Quinolinium 3, 5-dinitrobenzoate: a novel third order non-linear optical material for optoelectronic applications, *Spectrochim. Acta, Part A*, 2021, **249**, 119304.

99 L. Mydlova, S. Taboukhat, K. Waszkowska, N. Ibrahim, A. Migalska-Zalas, B. Sahraoui and M. Makowska-Janusik, Selected molecules based on (-1-cyanovinyl) benzonitrile as new materials for NLO applications—Experimental and computational studies, *J. Mol. Liq.*, 2020, **314**, 113622.

100 S. Ahmed, X. Jiang, C. Wang, U. E. Kalsoom, B. Wang, J. Khan and H. Zhang, An Insightful Picture of Nonlinear Photonics in 2D Materials and their Applications: Recent Advances and Future Prospects, *Adv. Opt. Mater.*, 2021, **9**(11), 2001671.

101 D. H. Williams, E. Stephens, D. P. O'Brien and M. Zhou, Understanding noncovalent interactions: ligand binding energy and catalytic efficiency from ligand-induced reductions in motion within receptors and enzymes, *Angew. Chem. Int. Ed.*, 2004, **43**(48), 6596–6616.

102 G. Han, X. Zhao and A. Farajtabar, Equilibrium Solubility and Solvent Effect Study of 3-Nitrosalicylic Acid in Different Monosolvents Covering Temperatures from 278.15 to 323.15 K, *J. Chem. Eng. Data*, 2021, **66**(7), 2882–2894.